Redefining Uncertainty: A Complete Bayesian Workflow for Ocean Color Remote Sensing

Erdem M. Karaköylü[a]

[a]*Independent Consultant, University Park, Maryland, 20782, USA*

Abstract

Traditional satellite ocean color algorithms for chlorophyll-a and inherent optical property retrieval rely on deterministic regression models that typically produce single-point predictions without explicit uncertainty quantification. The absence of uncertainty awareness undermines in-situ/model match-ups, reduces predictive reliability, and ultimately erodes user confidence. In the present study, I address this limitation by demonstrating how to implement a complete Bayesian workflow applied to the foundational chlorophyll-a retrieval problem. To that end, I use a set of well-established Bayesian modeling tools and techniques to train and evaluate probabilistic models that approximate the underlying data-generating process and yield posterior distributions conditioned on both data and model structure. The posterior distribution is an information-rich construct that can be mined for diverse insights. I develop and compare models of increasing complexity, beginning with a baseline polynomial regression and culminating in a hierarchical partial pooling model with heteroscedasticity. Similar to classical machine learning, model complexity in a Bayesian setting must also be scrutinized for its potential to overfit. This is addressed through efficient cross-validation and uncertainty calibration that exploit the full posterior distribution. Within this framework, the most complex model performed best in terms of out-of-sample uncertainty calibration and generalizability. Persistent localized mismatches across models point to domains where predictive power remains limited. Taken together, these results show how placing uncertainty at the center of inference allows a Bayesian approach to produce transparent, interpretable, and reliable chlorophyll-a retrievals from satellite ocean color data, paving the way for the development of more

Email address: erdemk@protonmail.com (Erdem M. Karaköylü)

robust marine ecosystem monitoring products.

Keywords: Ocean color remote sensing; Uncertainty quantification; Bayesian modeling workflow.

---

1. Introduction

Satellite ocean color remote sensing has long served as a cornerstone of marine ecosystem monitoring, offering global and synoptic coverage of surface ocean properties. Among these, chlorophyll-a (Chl_a) concentration remains a central quantity, widely used as a proxy for phytoplankton biomass, primary production and water quality. The retrieval of Chl_a from ocean color data has evolved over decades, resulting in a diverse lineage of empirical and semi-empirical algorithms. The following section summarizes this historical development, which sets the stage for a critical examination of the statistical foundations underlying current approaches.

1.1. Background

Early empirical algorithms, notably the OCx family developed by O'Reilly et al. (O'Reilly et al., 1998; O'Reilly et al., 2000), established a statistical template for retrieving chlorophyll-a (Chl_a) concentration from ocean color data. These models relate log-transformed blue-to-green reflectance ratios to in situ Chl_a, utilizing either direct band ratios or maximum band ratios (MBR)—the latter selecting the largest blue-to-green ratio for a given observation and applying a high-order polynomial fit. Their empirical simplicity and practical robustness made these polynomial regressions the operational foundation for chlorophyll products across successive satellite sensors (e.g., CZCS, SeaWiFS, MODIS, MERIS). They proved particularly effective in Case-1 waters, where phytoplankton dominate the optical signal.

However, performance degrades in optically complex Case-2 waters, where non-phytoplankton components (e.g., suspended sediments, colored dissolved organic matter) disrupt the assumed reflectance–chlorophyll-a relationship. These models are also sensitive to atmospheric correction errors, particularly in the blue spectral region. More fundamentally, the OCx family reflects a deterministic, frequentist modeling tradition: it models the sampled data to produce single-point predictions with fixed coefficients, without formally quantifying parameter or predictive uncertainty.

Subsequent refinements have addressed these limitations. For example, the Color Index (CI) method (Hu et al., 2012) employs a band-difference approach to reduce sensitivity to sensor noise and atmospheric residuals. Ongoing efforts have led to newer algorithm variants such as OC5 and OC6 (O'Reilly and Werdell, 2019), which incorporate additional bands or modified ratio formulations to better capture variability across chlorophyll regimes.

1.2. Limitations of Existing Approaches

The development of traditional ocean color algorithms is grounded in a fundamental statistical error - one that pervades much of observational science: the conflation of sampling probability with inferential probability (Jaynes and Bretthorst, 2003; Scheemaekere and Szafarz, 2011).

Consider a data set D composed of input-output pairs, as is the case of remote sensing reflectance (Rrs) and chlorophyll-a concentration - and a model M, representing their relationship. The sampling probability $p(D|M)$ denotes the probability of observing data D under the assumption that model M is true. Standard model fitting whatever the specific form, is typically carried out by maximizing this likelihood: parameters are adjusted so that M best explains the observed data.

This practice tacitly assumes that the model that maximizes $p(D|M)$ also provides the best representation of the underlying data-generating process. This assumption is a fallacy: it treats the sampling probability $p(D|M)$ as if it were the inferential probability $p(M|D)$. While in data-rich well-behaved settings the two may coincide, this is the exception rather than the rule. As Clayton (2022) argues, this misinterpretation lies at the heart of what he terms *Bernoulli's Fallacy*: the widespread tendency to equate likelihood with inference. The consequences of this logical misstep extend well beyond science for medicine, law, and public policy.

In practical terms, the fallacy underlies poor model generalization, drives the use of ad hoc, retrospective uncertainty quantification, and contributes to published findings that subsequently prove difficult to replicate Baker (2016); Cobey et al. (2024). These limitations are not restricted to classical hypothesis testing; they persist in the training and deployment of modern machine learning models as well.

This concern has been repeatedly raised in the machine learning literature. Gal (2016) and Ghahramani (2015) argue that most ML models discard uncertainty altogether. The result is overconfident predictions and brittle generalization, a dynamic echoed more broadly in remote sensing where neglecting uncertainty has been shown to undermine the reliability and interpretability of derived products (Werther and Burggraaff, 2023). Bishop (2006) similarly distinguishes between the utility of predictive models and the inferential scaffolding required to quantify uncertainty, reinforcing the notion that likelihood alone is insufficient.

This likelihood-centered training paradigm is typically framed as maximizing likelihood or, equivalently minimizing negative log likelihood or some other loss function. When models are parameterized only to output a scalar (e.g., a regression mean), such training produces point predictions with no uncertainty. When structured to output a full predictive distribution (e.g. Gaussian mean and variance), log-likelihood fitting can capture aleatoric uncertainty under the assumed noise family. In either case, optimization yields a single best parameter vector, providing no account of epistemic uncertainty about parameters or model structure (Ghahramani, 2015; Gruber et al., 2025). In practice, predictive variability can be approximated through heuristic methods such as deep ensembles and Monte Carlo dropout, which mimic epistemic uncertainty by injecting stochasticity into training and inference. More principled approaches such as MCMC sampling and variational inference combine explicit priors with likelihoods to yield posterior distributions with well-defined probabilistic semantics.

1.3. Overcoming Limitations

In oceanographic remote sensing, several recent efforts have attempted to address the limitations of classical models. For instance, Seegers et al. (2018) proposed alternative evaluation metrics to move beyond restrictive frequentist assumptions. Others have introduced Bayesian elements into the modeling pipeline: Frouin and Pelletier (2015) applied Bayesian inversion for atmospheric correction, Shi et al. (2015) used probabilistic fusion for multi-sensor data, and Craig and Karaköylü (2019) employed Hamiltonian Monte Carlo to train Bayesian neural networks (BNNs) for retrieving inherent optical properties (IOPs) from top-of-atmosphere radiance. Similarly, Werther et al. (2022)

used Monte Carlo dropout to approximate Bayesian inference in IOP retrieval, while Werther et al. (2025) benchmarked multiple probabilistic neural network architectures for quantifying aleatoric and epistemic uncertainty. Erickson et al. (2023) recast the Generalized Inherent Optical Property (GIOP) framework using conjugate Bayesian linear models.

These and other studies mark important progress. However, as Werther and Burggraaff (2023) emphasize, embracing uncertainty requires more than scatter plots with error bars. Despite growing interest in Bayesian tools for ocean color modeling, the full Bayesian workflow (Gelman et al., 2020; Wolkovich et al., 2024) remains underutilized. More commonly, probabilistic components are added to otherwise frequentist pipelines, without addressing the underlying definition of uncertainty.

In the ocean color community, uncertainty is most commonly defined following the GUM convention (JCGM, 2008) as a parameter characterizing the dispersion of values that could reasonably be attributed to the measurand (Tilstone et al., 2020). This frequentist view emphasizes measurement variability, typically expressed through standard deviations or confidence intervals, based on assumptions about repeated sampling and error propagation.

By contrast, in the Bayesian framework, uncertainty is defined as the probability distribution over unknown quantities, conditional on the observed data and the model used to represent the process (Ghahramani, 2015; Gelman et al., 2020; Gruber et al., 2025). Aleatoric uncertainty corresponds to the conditional variability of outcomes $Var(Y|X = x)$, while epistemic uncertainty reflects limited knowledge of parameters, model structure or data quality. A Bayesian credible interval therefore represents a direct probabilistic statement - e.g., "there is an 89% probability that the true value lies in this interval, given the data and model - and its width can and should be tailored thoughtfully to scientific or decision-making relevance.

Bridging this gap requires more than Bayesian components; it requires Bayesian thinking. In what follows, I recast a foundational chlorophyll retrieval problem as a fully Bayesian workflow, where uncertainty is a central object of inference that quantifies what the practitioner does not know about the underlying data-generating process.

2. Materials and Methods

2.1. Dataset, Preprocessing and Feature Engineering

I used the familiar NASA Ocean Biology Processing Group's NOMAD dataset (Werdell and Bailey, 2005), which contains quality-controlled in situ chlorophyll-a measurements matched with satellite-derived remote sensing reflectance (Rrs) observations. The dataset spans a wide range of oceanographic conditions, enabling model development with potential for broad generalization.

I retained visible Rrs bands from SeaWiFS (411, 443, 489, 510, 555, and 670 nm) and removed observations with invalid (null, zero, or negative) values. Chlorophyll-a concentrations measured using HPLC or fluorescence were log-transformed using base 10, consistent with ocean color convention. The same base-10 log transformation was applied to MBR and other predictors. Unless otherwise noted, log refers to $\log_{10}$ throughout this manuscript.

To construct the primary predictor, I computed the Maximum Band Ratio (MBR), following the OC6 formulation of O'Reilly and Werdell (2019), which uses the maximum of blue bands relative to a green/red denominator (555 and 670 nm). In this implementation, the denominator is taken as the sum of Rrs(555) and Rrs(670); using the mean, as in O'Reilly et al., is equivalent up to a constant factor and has no effect after log transformation.

$$MBR = \frac{\max(Rrs_{411}, Rrs_{443}, Rrs_{489}, Rrs_{510})}{Rrs_{555} + Rrs_{670}}$$

I then created a categorical grouping variable,based on which numerator band was dominant for each observation. This is used in Models 2-5 providing group-specific formulation that improve model adaptability.

2.2. Modeling Approach

I developed a sequence of Bayesian regression models to estimate log-transformed chlorophyll-a from log-transformed MBR. Models were implemented using PyMC v5 (Abril-Pla et al., 2023). Prior to training, model assumptions - expressed as priors on model coefficients - were verified through Prior Predictive Checks to see if the model was able to generate reasonable predictions

before exposure to data. If deemed necessary, priors were adjusted. For model fitting, I used the No-U-Turn Sampler - NUTS, (Homan and Gelman, 2014) - an adaptive variant of Hamiltonian Monte Carlo; itself a state-of-the-art Markov Chain Monte Carlo (MCMC) algorithm. I assessed convergence using Gelman-Rubin's $\hat{R}$ diagnostic, effective sample size (ESS), and visual trace plot inspection (McElreath, 2020). $\hat{R}$ measures how well independent MCMC chains converge; a value of 1.00-1.01 is indicative of good convergence. ESS estimates how much independent information is available for each model parameter in potentially autocorrelated MCMC chains; ESS greater than 1000 suggests stable estimates. Both metrics are suggestive, and unmet criteria are not necessarily deal breakers but call for heightened vigilance.

Once trained each model's predictive skill was evaluated using several approaches. The first uses Posterior Predictive Checks (PPC). Similar to prior predictive checks, this compares training data to trained model simulated output.

Models were then evaluated for generalization (how well they can predict on out-of-sample data) and uncertainty calibration (how realistic prediction uncertainties are). For this I used the Leave-One-Out cross validation (LOO) Probability Integral Transform (PIT); LOO-PIT Säilynoja et al. (2022), which has been applied in variety of fields including astrophysics, epidemiology, genetics (*cf.* Nguyen et al. 2025). The PIT definition states that if a random variable X has a continuous distribution with cumulative distribution function (CDF) F_X, then the random variable $Y = F_X(X)$ is uniformly distributed. In LOO-PIT, the model is fit on all but one observation, and the CDF of the posterior predictive distribution is used to compute the PIT for the held-out value. If the model is well-calibrated, the PIT values should follow a uniform distribution. A more detailed explanation of the method and its implementation is provided in the Supplementary Materials. To reduce computational complexity, LOO does not require refitting the model for each data point. Instead, it uses a Pareto Smoothed Importance Sampling (PSIS, Vehtari et al. 2024) approximation, which re-weights draws from the full posterior to approximate leave-one-out posteriors in a stable and efficient manner (Vehtari et al., 2016). The approach include diagnostics to highlight potential issues with the approximation.

PSIS-LOO also yields a scalar metric for model comparison: the expected log predictive density

(ELPD, Vehtari et al. 2016). This quantity summarizes how well a model is expected to predict new data. Models with higher ELPD values are preferred. In practice, I compared models by their ELPD and corresponding standard errors, and considered differences significant when the ELPD gap exceeded its uncertainty. In combination with the previously described analysis steps, this provides a robust, fully Bayesian approach to selecting among competing models.

Finally, I computed predictive interval coverage: the proportion of observed values falling within the 94% highest density intervals (HDI - the narrowest possible interval) of the posterior predictive distribution. This was done for both in-sample and out-of-sample datasets to assess generalization. A SeaBASS matchup dataset, containing 53 clean and complete observations after preprocessing, was used for out-of-sample-validation.

The choice of a 94% HDI, rather than a conventional 95%, is deliberate. In Bayesian modeling, interval width is not bound to fixed conventions but should be selected to reflect the modeling context and decision-making needs. This serves as a reminder that credible intervals are probabilistic statements whose interpretation is meaningful only when their level is chosen intentionally, not dogmatically.

2.2.1. Model Progression

Modeling proceeded iteratively. Initial model performance and diagnostics motivated refinement that led to a total of 5 models, hereafter referred to as Models 1–5. For clarity and parsimony, only Models 1, 2, and 5 are presented in the main text; intermediate variants, Models 3 and 4, are described and analyzed in the Supplementary Materials. Table 1 summarizes the three main models discussed in the main text.

Table 1: Summary of model progression. Each model incrementally addresses limitations in structure or variance.

Model	**Type**	**Key Characteristics**
Model 1	Polynomial Regression	Bayesian re-framing of OCx (OC6-style), with a 4th-order polynomial on log(MBR) predicting log(Chl)
Model 2	Hierarchical Linear Regression (HLR)	Partial pooling across MBR numerator groups, each with its own intercept and slope
Model 5	Heteroscedastic HLR	Extends Model 2 by modeling log(σ) as a linear function of log(MBR), with group-specific slopes and intercepts.

2.2.2. Model Structures and Priors

Model 1 uses a single-level polynomial structure with Gaussian priors on all regression coefficients and a Gamma prior on the shared dispersion parameter σ. Model 2 introduces a hierarchical structure with group-specific slopes and intercepts based on the dominant MBR numerator band. Unlike the 4th-order polynomial used in Model 1, this model uses a simple linear form and shares information across groups through partial pooling. This added structure is expected to capture spectral variability more effectively and yield improved calibration. Model 5 adds heteroscedasticity by modeling $log(\sigma_i)$ as a linear function of log(MBR), with group-specific slopes and intercepts.

All group-level parameters were given Normal priors centered at zero, and hyper-prior standard deviations followed Exponential(1) distributions to allow regularization via partial pooling. Prior predictive checks were performed for all models to ensure reasonable behavior before fitting.

Figure 1 shows the structure of Model 1 as a directed acyclic graph (DAG). DAGs for Models 2 and 5 are provided in the Supplementary Material.

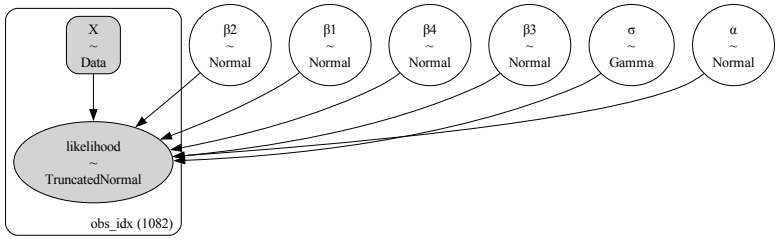

Figure 1: Model 1 Directed Acyclic Graph (DAG). Gaussian priors are used for the intercept α and polynomial coefficients β_1–β_4. The dispersion parameter σ is given a weakly informative, Gamma prior restricted to positive values. Observations are modeled via a truncated normal distribution, constraining log(Chl) to ecologically and instrumentally plausible ranges.

The next section presents results for Models 1, 2, and 5. Extended analyses and diagnostics for all models, including Models 3 and 4, are provided in the Supplementary Materials.

3. Results

3.1. Model Performance Overview

Three models were fit to the data, each extending the previous in structural complexity. Model 1, a Bayesian analogue of OCx-style 4^{th} order polynomial regression, served as a baseline. Model 2 introduced group-specific structure via hierarchical partial pooling by dominant MBR numerator band. Model 5 extended Model 2 by introducing heteroscedasticity, allowing the dispersion parameter to vary with log(MBR) across groups.

3.2. Model Evaluation: Prior Predictive, Posterior Predictive, and LOO-PIT

Standard evaluation metrics such as R^2 or RMSE assess how closely point predictions match observed data. However, these are not appropriate for complete Bayesian model evaluation. These models yield full posterior distributions rather than single-value estimates. Moreover the goal is to approximate the data generation process, not to model data. In this context, predictive accuracy must be judged not only by central tendency but also by how well the model represents uncertainty.

To that end, I evaluate each model using prior and posterior predictive checks and LOO-PIT diagnostics, which respectively assess in-sample fit and out-of-sample calibration. These diagnostics are presented below for Models 1, 2, and 5, beginning with Model 1.

3.2.1. Model 1: Polynomial Regression

The top two panels in Figure 2 display kernel density estimates (KDEs) comparing simulated and observed distributions of log-transformed chlorophyll-a. KDEs provide smoothed estimates of probability density, used to assess how well the model reproduces observed distributions.

The top-left panel shows the prior predictive distribution. Simulated draws from the model under the prior (gray lines) span a wide range of values, as expected given the weakly informative priors. The mean of these simulations (orange dashed line) is diffuse and relatively flat, indicating that the prior allows the model to generate a wide range of plausible outcomes. The observed data KDE (black line) does not influence the prior predictive draws, as the model has not yet been trained on the data; it is included here solely to facilitate comparison with the posterior predictive check in the top-right panel.

The top-right panel compares the posterior predictive distribution to the same observed KDE. The black line represents the empirical distribution of the data, estimated from the NOMAD dataset. It is unimodal, with a dominant peak near log(Chl) = 0 (i.e., 1 mg m^{-3}), typical of mesotrophic or moderately productive coastal waters. A secondary shoulder appears near log(Chl) $\approx$ -0.5, corresponding to lower chlorophyll concentrations (0.3 mg m^{-3} and below) associated with oligotrophic oceanic regions. This structure indicates that the dataset includes a range of ecological regimes, with a skew toward oceanic conditions.

Posterior predictive draws (gray lines) cluster tightly around the observed KDE and differ markedly from the diffuse prior predictive draws, suggesting that the model has learned meaningfully from the data. The posterior predictive mean (orange dashed line) successfully captures the overall support and central tendency of the observed distribution. However, it underestimates the height of the primary mode, and assigns excess probability mass to the shoulders, yielding a flattened peak. This suggests that while the model captures the broad structure of the data, it

produces overdispersed predictions, with intervals that are too wide relative to the concentration of observations.

The bottom two panels assess model calibration using leave-one-out probability integral transform (LOO-PIT) diagnostics. Two complementary views are shown: the left panel presents the density of LOO-PIT values via a kernel density estimate (KDE), while the right panel shows the cumulative deviation of those values from the ideal uniform distribution. The KDE is sensitive to local concentration of probability mass—such as over- or underdispersion—while the ECDF-minus-uniform plot emphasizes systematic calibration drift across the distribution. Together, they provide a more complete picture of model uncertainty than either view alone.

The KDE panel (bottom-left) shows the LOO-PIT density (black line) compared against 500 KDEs of values drawn from a uniform distribution (thin blue lines). A horizontal dashed line at $y = 1$ denotes the target density for a calibrated model. The observed KDE exhibits a distinct U-shape, with density elevated in the tails and suppressed in the center. This pattern confirms that the model is likely to be **overdispersed** in out-of-sample prediction: its predictive intervals are too wide, placing too little mass near the typical observations and too much in the extremes.

The bottom-right panel displays the ECDF difference plot, created by subtracting the expected theoretical CDF values (the identity function in [0,1] for standard uniformity) from the observed ECDF values. A horizontal dashed line at $y = 0$ references a lack of difference. The shaded band shows a 94% credible interval for this difference under ideal conditions, based on repeated uniform draws. The curve for Model 1 deviates below the reference line in the central quantiles and rises above it in the tails, confirming the pattern seen in the KDE panel. Together, these diagnostics show that while Model 1 captures the central trend of the data, its posterior predictive distributions are too diffuse.

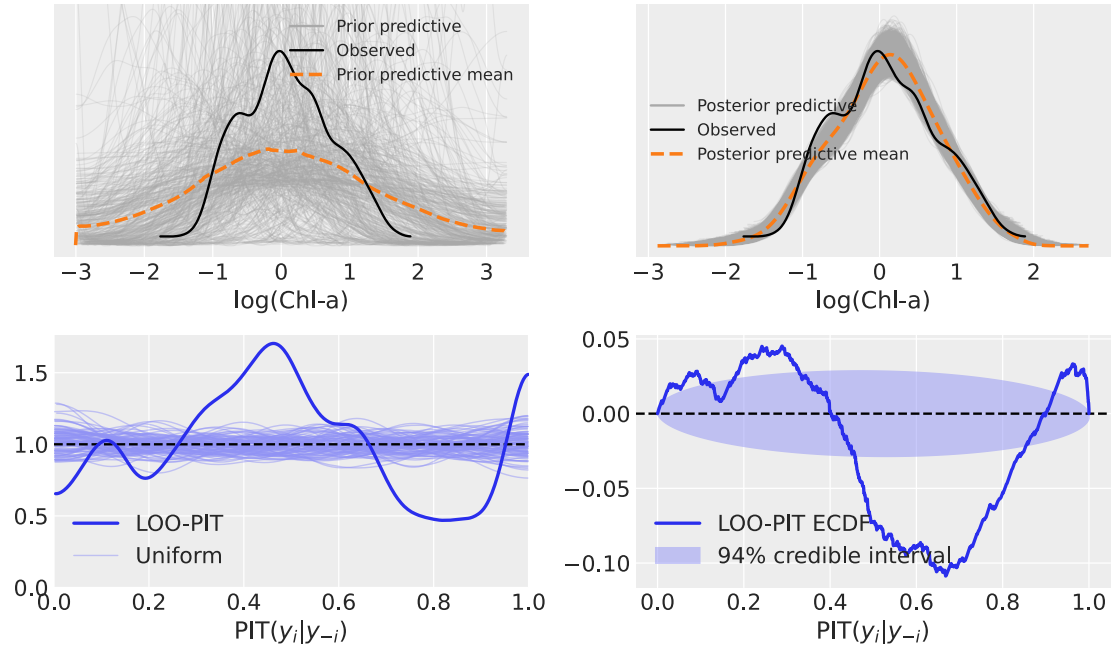

Figure 2: Model 1: Top row shows prior and posterior predictive distributions. Bottom row shows model calibration assessed using LOO-PIT plots. Left panel shows the kernel density estimate (KDE) of the LOO-PIT values. For a well-calibrated model, the distribution should be approximately flat, indicating that observed outcomes are consistent with the posterior predictive distributions. Deviations from flatness, such as peaks or dips, reflect under- or overconfidence in different parts of the predictive distribution. The right panel shows the difference between the empirical cumulative distribution function (ECDF) of the LOO-PIT values and the ideal uniform CDF. Deviations from zero indicate miscalibration: values below zero in central quantiles reflect underprediction, while values above zero in the tails reflect overprediction.

3.2.2. Model 2: Hierarchical Linear Regression

Figure 3 shows the model evaluation panels for Model 2. The prior predictive simulations (top-left) are broader than in Model 1, reflecting the additional flexibility introduced by the hierarchical structure. The prior predictive mean is diffuse, consistent with weakly informative priors to allow for a wide range of generative behaviors.

The posterior predictive check (top-right) shows a notable improvement over Model 1. Posterior draws cluster tightly around the observed KDE, especially near the primary mode. This reflects the effect of partial pooling across MBR groups, which concentrates predictions around dominant patterns in the data. However, the model fails to fully capture the secondary shoulder near log(Chl) ≈ -0.5, suggesting that some variation remains unaccounted for — possibly due to

shrinkage of uncertainty toward the group mean.

As with Model 1, LOO-PIT diagnostics assess out-of-sample calibration. The KDE reveals local deviations from calibration, while the ECDF-minus-uniform plot captures cumulative miscalibration trends. Here, the LOO-PIT diagnostics (bottom row) further support the improved performance. The KDE panel (bottom-left) shows smaller deviations from the uniform reference (dashed line at $y = 1$) compared to Model 1. The y-axis range here is narrower—approximately 0.5 to 1.3—indicating that the magnitude of miscalibration is significantly reduced. Similarly, the ECDF-minus-uniform plot (bottom-right) shows deviations that remain well within the 94% credible interval, with a y-axis span of just ± 0.025. These compressed ranges reflect a more calibrated model. Mild signs of overdispersion persist—visible as a small negative dip in the central quantiles—but overall, Model 2 represents a substantial improvement in both fit and uncertainty calibration relative to the baseline.

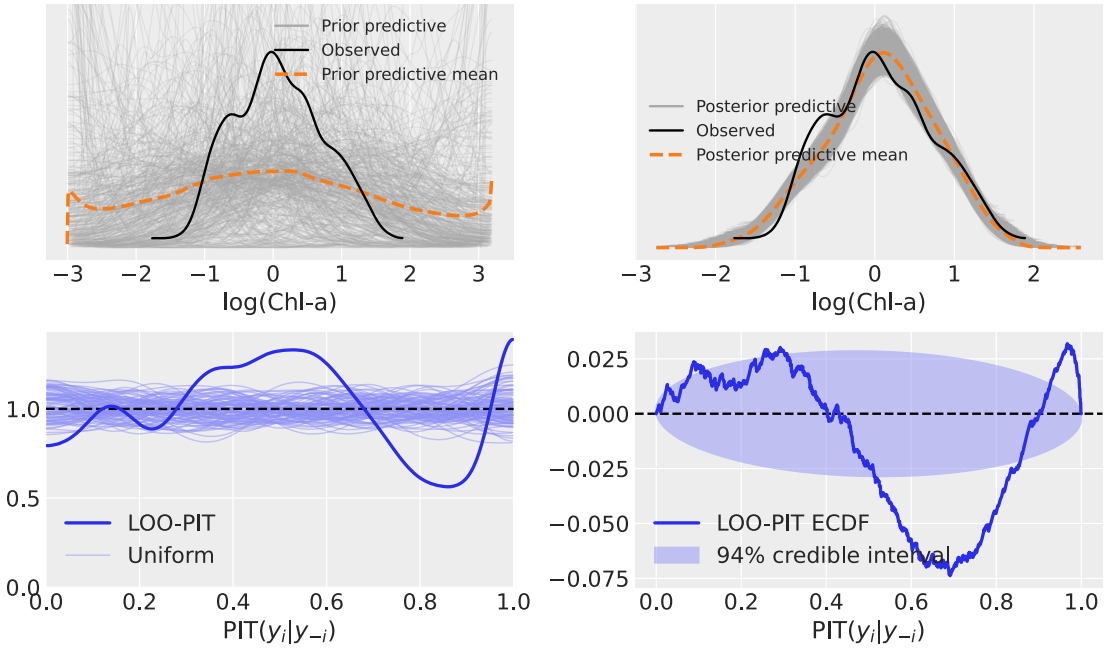

Figure 3: Model 2: Prior/posterior predictive checks (top), LOO-PIT diagnostics (bottom), showing improved calibration relative to Model 1 with only mild overdispersion.

3.2.3. Model 5: Heteroscedastic Hierarchical Linear Regression

Model 5 extends the hierarchical structure of Model 2 by allowing the likelihood variance σ to vary linearly with log(MBR), using group-specific intercepts and slopes. This accommodates heteroscedasticity across spectral groups and better reflects the variance structure of the data. By explicitly modeling the dispersion, the model is expected to improve both fit and calibration, particularly in the tails of the predictive distribution.

Figure 4 presents the four-panel evaluation for Model 5. The prior predictive simulations (top-left) are the most diffuse of any model—expected, given the added flexibility in both the mean and variance components. The prior predictive mean (orange dashed line) is nearly flat. As before, the observed KDE (black line) is included only for visual comparison. The posterior predictive check (top-right) shows excellent agreement between the posterior draws and the observed KDE. The model captures both the main mode near log(Chl) = 0 and the secondary shoulder near -0.5—something neither Model 1 nor 2 accomplished. The predictive mean aligns closely with the observed distribution, and the vertical spread among draws reflects uncertainty in both the mean and variance terms.

For Model 5 the bottom-left LOO-PIT panel shows a nearly flat density centered around the ideal reference line at $y = 1$, with minor undulations well within the light blue band representing draws from the uniform distribution. The vertical range is now the tightest of all three models and indicates minimal deviation from ideal calibration. The ECDF deviance (bottom-right panel) shows similarly tight behavior. The LOO-PIT curve remains entirely within the 94% credible interval and deviates by no more than ± 0.02 from the reference line at $y = 0$. Together, these diagnostics suggest that Model 5 is the best calibrated and most accurate of all models developed in this study.

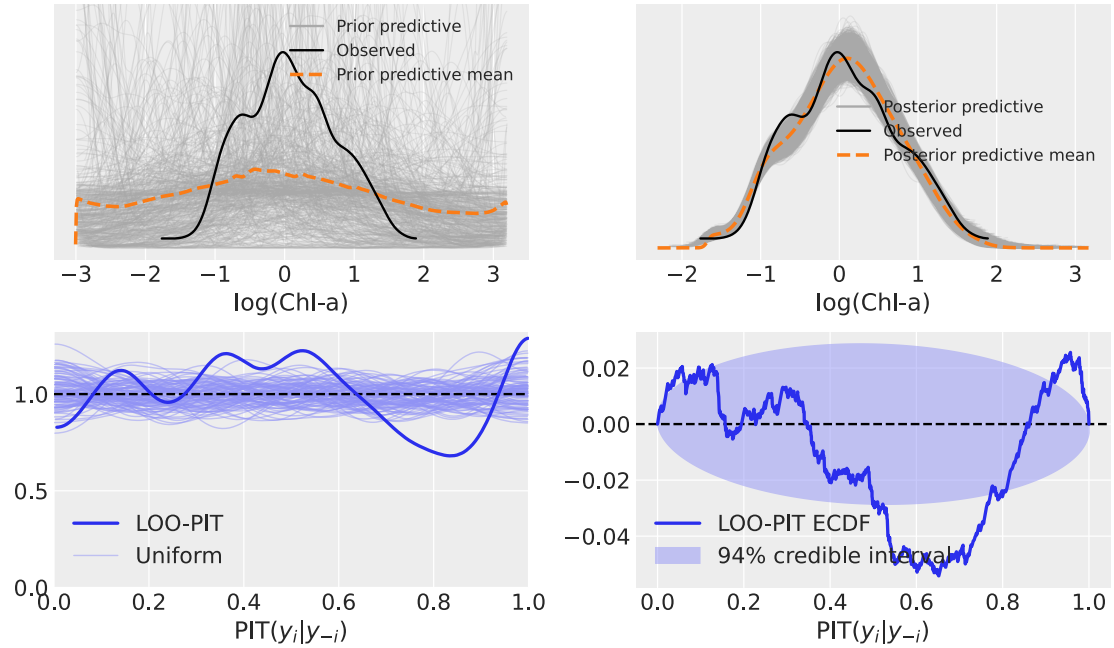

Figure 4: Model 5: Prior/posterior predictive checks (top), LOO-PIT diagnostics (bottom), showing the best fit and calibration of all models.

3.3. Predictive Coverage

Posterior predictive intervals represent a core strength of Bayesian modeling: the ability to express uncertainty in probabilistic terms. A 94% highest density interval (HDI) reflects a direct statement about the distribution of predicted outcomes:

"Given a specific input, there is a 94% probability that the outcome lies within this interval, conditioned on the model and the data."

This stands in contrast to frequentist confidence intervals or classical machine learning point predictions, which provide no such probabilistic guarantee. Instead of merely reporting central tendencies or summary error metrics, Bayesian predictive intervals communicate how confident the model is about each individual prediction.

Figures 5–7 visualize this by overlaying 94% HDI on scatter plots of observed log-transformed chlorophyll-a concentrations. Shaded ribbons represent the predicted HDI at each value of log(MBR), stratified by MBR numerator group. If a model represents the data-generating process well, the HDI

should envelop the bulk of the observations, adjusting their width to reflect changes in uncertainty across the covariate space.

This kind of distribution-aware predictive structure is essential in scientific contexts like ocean color remote sensing, where quantifying uncertainty is as important as making accurate predictions.

3.3.1. Model 1

Figure 5 shows the 94% posterior predictive intervals from Model 1 overlaid on the observed log-transformed chlorophyll-a values, stratified by dominant MBR numerator band. Because this model uses a constant dispersion term (σ), the predictive intervals maintain a uniform width across log(MBR), regardless of local data density or group-specific trends.

In the in-sample (NOMAD) panel, the HDI bands roughly follow the central trend of the data but ignore group-specific patterns. Some groups are captured in the middle of the log(MBR) range, but coverage deteriorates in the tails, where intervals are either too wide or too narrow depending on the group.

In the out-of-sample (SeaBASS) panel, the model often fails to cover held-out observations, particularly at low and high values of log(MBR). A cluster of six Rrs(489) group observations falls below the 94% HDI band.

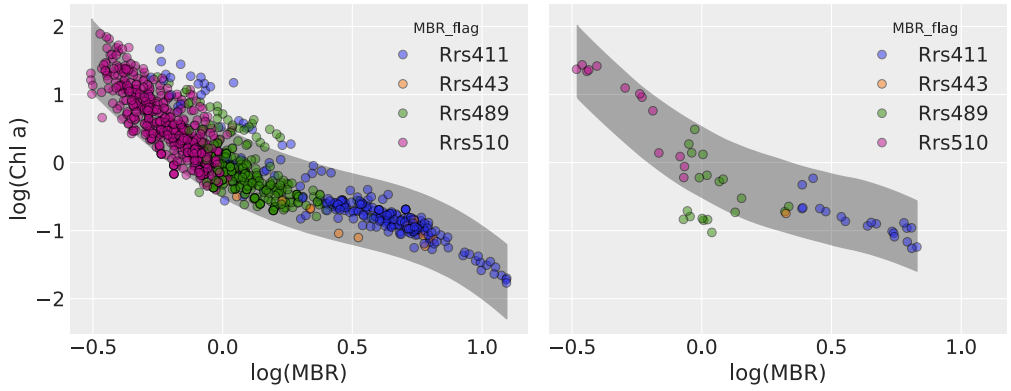

Figure 5: Model 1 predictive coverage plots. Left: in-sample (NOMAD). Right: out-of-sample (SeaBASS). The gray envelope shows the 94% posterior predictive highest density interval (HDI). Scatter points are observed values. Model 1 does not incorporate group structure, and points are colored by dominant MBR numerator band for reference only.

3.3.2. Model 2

Figure 6 shows predictive coverage plots for Model 2, which introduces group-specific linear fits via a hierarchical structure. This partial pooling allows the model to share information across MBR numerator groups while still learning distinct intercepts and slopes for each.

In the in-sample coverage, the HDI bands now reflect different mean relationships across groups. This better matches the stratified nature of the data and corrects for the uniformity of the polynomial fit in Model 1. However, the interval width remains constant within each group, as the model still uses a shared, homoskedastic dispersion term. As a result, although the predicted means improve, the HDI bands still fail to capture group-specific differences in variance.

In the SeaBASS panel, the model shows improved group-wise trend fitting, but the same Rrs(489) cluster remains outside the HDI range, as in Model 1.

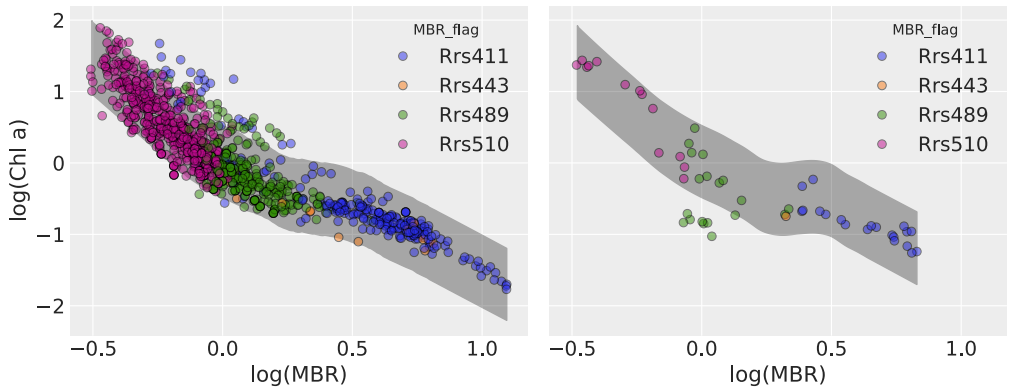

Figure 6: Model 2 predictive coverage plots. Left: in-sample (NOMAD). Right: out-of-sample (SeaBASS). The gray envelope shows the 94% posterior predictive highest density interval (HDI) for each MBR numerator group, with group-specific fits modeled explicitly. Scatter points are observed values, colored by dominant MBR numerator band. Compared to Model 1, Model 2 captures group-specific mean relationships more effectively but retains constant-width intervals, failing to represent variance differences across groups.

3.3.3. Model 5

Figure 7 shows the predictive coverage for Model 5, which retains the group-specific linear structure of Model 2 and introduces heteroscedasticity by modeling $\log(\sigma)$ as a linear function of log(MBR), with group-specific intercepts and slopes. This structure allows the posterior predictive intervals to vary in both shape and width across the predictor space and between groups.

In the NOMAD dataset (left panel), the HDI bands closely follow the observed spread for most groups and values of log(MBR), suggesting that the model has captured both the mean trends and variance structures. However, two points belonging to the Rrs(443) group fall below the lower edge of the 94% HDI, indicating that the model slightly overestimates chlorophyll-a for these observations. While localized, these deviations highlight that even overall better calibrated models may still fail to capture rare configurations within a group.

In the SeaBASS dataset (right panel), Model 5 shows overall strong alignment between predictive intervals and held-out observations. The HDI bands vary in shape and width across log(MBR) and MBR groups, indicating that the model has captured key aspects of input-dependent variance. Most groups show good coverage across the covariate range.

However, as with Models 1 and 2, a cluster of six observations in the Rrs(489) group consistently falls below the 94% HDI band. The shape of the HDI does not adjust to encompass these points, suggesting a consistent mismatch between predicted and observed values for this subset of the test data.

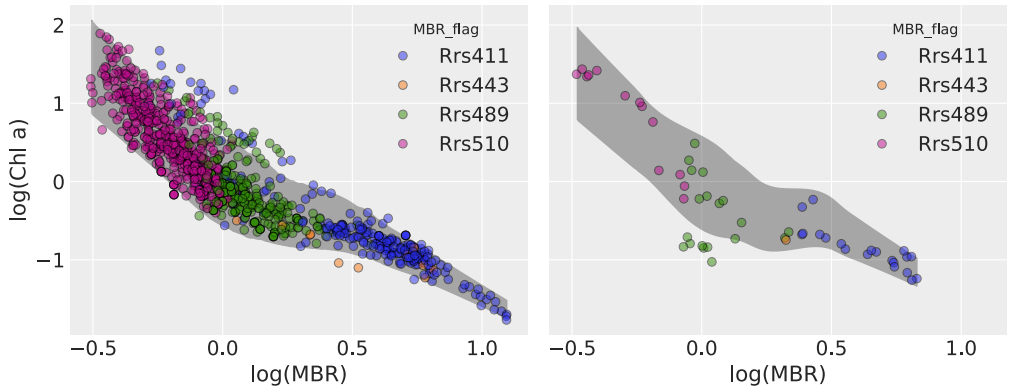

Figure 7: Model 5 predictive coverage plots. Left: in-sample (NOMAD). Right: out-of-sample (SeaBASS). The gray envelope shows the 94% posterior predictive highest density interval (HDI), with both mean structure and variance allowed to vary as a function of log(MBR) within each MBR numerator group. Scatter points are observed values, colored by dominant MBR numerator band. Model 5 achieves the best overall predictive coverage, with intervals adapting in both width and shape across groups, although localized mismatches (e.g., some Rrs(443) and Rrs(489) points) remain.

Overall, each increase in model complexity yielded clear improvements in predictive performance. Model 2 corrected the uniform mean structure of Model 1 by incorporating group-specific

fits, though its constant-width intervals failed to capture variance differences. Model 5 extended this framework with heteroscedasticity, allowing both mean and variance to vary across groups, and achieved the best overall predictive coverage. Nonetheless, localized mismatches—such as the persistent Rrs(489) cluster—remained, underscoring the limits of even the most flexible model considered here.

3.4. Model Comparison

PSIS-LOO results are summarized in Table 2 and visualized in Figure 8. Among the three models evaluated, Model 5 achieved the highest expected log predictive density ($\mathrm{ELPD_{LOO}}$), indicating the best expected out-of-sample predictive performance. Model 2 ranked second, with an ELPD difference of 113.39 relative to Model 5, while Model 1 ranked third with an ELPD difference of 143.94. Model complexity is represented by the effective number of parameters (p_{loo}), which quantifies the model's flexibility as estimated from the posterior distribution. This measure is derived from the variance in the pointwise log-likelihood and reflects the degree to which the model adapts to the observed data. Across the three models, p_{LOO} increased from 5.32 in Model 1 to 15.55 in Model 5. Model 5 also had the highest model weight (0.96), indicating strong preference under the PSIS-LOO criterion.

Table 2: Model comparison using PSIS-LOO. Higher ELPD indicates better expected out-of-sample predictive performance. ΔELPD shows differences relative to the best model (Model 5). p_{loo} is the effective number of parameters, used as a measure of model complexity, and estimated from the variance in the pointwise log-likelihood. SE is the standard error of the ELPD estimate for each model. dSE is the standard error of the ΔELPD value between a given model and the best-performing model.

Model	**Rank**	**$\mathrm{ELPD_{LOO}}$**	**$\mathrm{p_{LOO}}$**	**ELPD diff**	**Weight**	**SE**	**dSE**
Model 5	1	-0.53	15.55	0.00	0.96	28.08	0.00
Model 2	2	-113.92	9.77	113.39	0.00	27.58	12.53
Model 1	3	-144.47	5.32	143.94	0.04	31.64	21.64

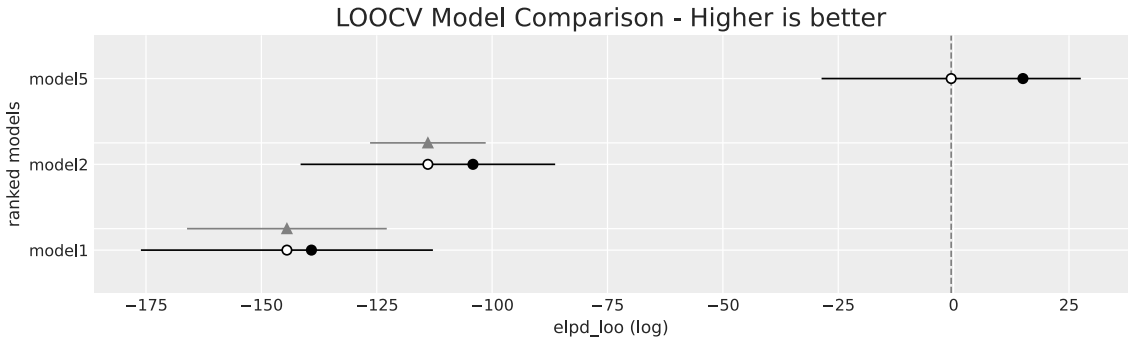

Figure 8: Model comparison plot showing differences in expected log predictive density (ΔELPD) and effective number of parameters (p_{loo}) for Models 1, 2, and 5. ΔELPD values are calculated relative to the best-performing model (Model 5), with higher ELPD indicating better expected out-of-sample predictive performance. Filled circles represent in-sample ELPD values from the posterior predictive distribution fit to all observations in the NOMAD dataset. Open circles represent out-of-sample ELPD values estimated using Pareto-smoothed importance sampling leave-one-out cross-validation (PSIS-LOO) applied to the same dataset. Both are expressed in the same log-probability units. Light gray horizontal lines indicate ± dSE (standard error of the ELPD difference) for each model relative to the best model. Triangles mark the best-performing model (ΔELPD = 0). Dark uncertainty bars correspond to the SE values reported in Table 2.

Overall, increasing model complexity was associated with improvements in calibration and predictive performance on aggregate diagnostics, while predictive coverage revealed a small number of localized deviations that persist across models; a cluster belonging to the Rrs(489) group of the out-of-sample data.

4. Discussion

4.1. Summary of Findings

This study demonstrates the application of a complete Bayesian workflow to a foundational ocean color chlorophyll-*a* retrieval problem. Building from a Bayesian analogue of the OCx-style polynomial regression, I progressively increased model complexity by introducing hierarchical structure across maximum band ratio (MBR) groups (Model 2) and subsequently allowing heteroscedasticity via group-specific variance models (Model 5). Across all evaluation metrics—prior and posterior predictive checks, LOO-PIT calibration diagnostics, predictive coverage, and PSIS-LOO model comparison—each successive model displayed measurable improvements in calibration and predictive accuracy. Model 5, the most complex in the series, achieved the highest expected log predictive density and the most consistent calibration across both training and held-out data.

While overall calibration improved with model complexity, localized deviations remained. In particular, a cluster of six Rrs(489) points from the SeaBASS dataset fell below the 94% highest density interval (HDI) across all models, and two Rrs(443) points in NOMAD moved outside the HDI in Model 5 despite being covered in simpler models. These exceptions highlight the need for targeted model extensions to fully capture structured predictive mismatches.

4.2. Comparison with Classical and Machine Learning Approaches

Unlike traditional chlorophyll-a retrieval algorithms or classical machine learning regressors, the Bayesian models presented here yield full posterior distributions over parameters and predictions. This framework enables direct probabilistic statements about prediction intervals—e.g., "given the data and model, there is a 94% probability that the true value lies within this interval"—that are unavailable in frequentist point-estimation frameworks.

Evaluation metrics such as R^2, RMSE, or MAE, commonly used in both classical regression and ocean color algorithm validation (Seegers et al., 2018), measure only point-prediction accuracy. They neither leverage the full posterior distribution nor account for model complexity. By contrast, Pareto-smoothed importance sampling leave-one-out cross-validation (PSIS-LOO) evaluates predictive performance using the entire posterior and adjusts for model complexity via the effective number of parameters (p_{LOO}). This complexity penalty reduces the risk of overfitting and allows fairer comparison between models of differing flexibility, similar in spirit to but more robust than information criteria such as AIC.

Classical machine learning regression models, including ensembles such as random forests or boosting methods, can flexibly fit nonlinear relationships but typically discard uncertainty unless specifically extended (e.g., through ensembles, dropout, or Bayesian variants). In contrast, Bayesian models natively quantify both parameter and predictive uncertainty, providing calibrated probability statements rather than only central predictions or heuristic confidence estimates.

4.3. Sources of Predictive Mismatch

Inspection of predictive coverage plots revealed several persistent patterns of mismatch. Most notably, a group of six Rrs(489) points in the SeaBASS dataset consistently fell below the lower

bound of the 94% HDI for all models. This indicates a systematic bias for this subset that is not explained by the current grouping structure. In the NOMAD dataset, two Rrs(443) points fell below the HDI only in Model 5, suggesting that increased complexity can occasionally overfit certain relationships, leading to localized loss of coverage. Such patterns imply that the current grouping by dominant MBR numerator, while capturing important structure, omits additional sources of variance, likely tied to sensor-specific or environmental factors.

4.4. Future Directions

The patterns of predictive mismatch identified here point toward several avenues for extending the present modeling framework.

First, the hierarchical structure could be expanded to include additional grouping variables—notably satellite sensor type—while also allowing heteroscedasticity to vary across these new dimensions. Such an approach would help capture systematic offsets in the reflectance–chlorophyll relationship arising from differences in spectral response functions, radiometric calibration, or atmospheric correction methodology. Crossed or nested random effects could enable simultaneous partial pooling across MBR groups and sensor categories, while variance terms could flexibly adapt to subsets of the data that exhibit systematically different levels of uncertainty.

Second, incorporating the full interband covariance structure offers a promising path to improved predictions. By treating the set of relevant spectral bands as a multivariate predictor, the model could exploit correlations among reflectances to resolve cases where univariate MBR-based predictors are insufficient. This could be implemented either through a multivariate regression framework or via direct modeling of the joint distribution of spectral inputs.

Together, these extensions would enhance the model's ability to represent both the central tendency and the uncertainty of chlorophyll-a predictions, reducing systematic mismatches and further aligning predictive coverage with the underlying data-generating process.

4.5. Concluding Remarks

By recasting a foundational chlorophyll-a retrieval problem within a fully Bayesian framework, this study illustrates the value of a complete workflow that integrates prior predictive checks, pos-

terior predictive diagnostics, calibration assessment via LOO-PIT, and complexity-adjusted model comparison using PSIS-LOO. The results show that accounting for both group-level structure and heteroscedasticity can substantially improve predictive calibration and the representation of uncertainty. At the same time, persistent localized mismatches highlight opportunities for targeted model extensions, particularly through the inclusion of additional grouping variables and the exploitation of spectral covariance. Together, these refinements point toward more reliable and interpretable chlorophyll-a products from satellite ocean color data, supporting the broader goal of uncertainty-aware remote sensing for marine ecosystem monitoring. An additional advantage of the Bayesian approach is that existing posteriors can be updated as new data become available, ensuring that models remain current as observing systems and *in-situ* matchups continue to grow.

Declaration of Generative AI and AI-Assisted Technologies in the Writing Process

During the preparation of this work, the author used ChatGPT to help check for errors, inconsistencies, redundancies, and potential issues with the narrative flow. After using this tool, the authors reviewed and edited the content as needed and assume full responsibility for the content of the publication.

References

Abril-Pla, O., Andreani, V., Carroll, C., Dong, L., Fonnesbeck, C.J., Kochurov, M., Kumar, R., Lao, J., Luhmann, C.C., Martin, O.A., et al., 2023. Pymc: a modern, and comprehensive probabilistic programming framework in python. PeerJ Computer Science 9, e1516. URL: https://doi.org/10.7717/peerj-cs.1516, doi:10.7717/peerj-cs.1516.

Baker, M., 2016. 1,500 scientists lift the lid on reproducibility. Nature 533, 452–454. doi:10.1038/533452a.

Bishop, C.M., 2006. Pattern Recognition and Machine Learning. Springer.

Clayton, A., 2022. Bernoulli's Fallacy: Statistical Illogic and the Crisis of Modern Science. Columbia University Press. URL: https://books.google.com/books?id=BT4CzwEACAAJ.

Cobey, K.D., Ebrahimzadeh, S., Page, M.J., Thibault, R.T., Nguyen, P.Y., Abu-Dalfa, F., Moher, D., 2024. Biomedical researchers' perspectives on the reproducibility of research. PLoS biology 22, e3002870.

Craig, S.E., Karaköylü, E.M., 2019. Bayesian models for deriving biogeochemical information from satellite ocean color. EarthArXiv doi:10.31223/osf.io/shp6y.

Erickson, Z.K., McKinna, L.I.W., Werdell, P.J., Cetinić, I., 2023. Bayesian approach to a generalized inherent optical property model. Optics Express 31, 22790 – 22801. URL: https://doi.org/10.1364/oe.486581, doi:10.1364/oe.486581.

Frouin, R., Pelletier, B., 2015. Bayesian methodology for inverting satellite ocean-color data. Remote Sensing of Environment , 332–360doi:10.1016/j.rse.2014.12.001.

Gal, Y., 2016. Uncertainty in Deep Learning. Ph.D. thesis. University of Cambridge.

Gelman, A., Vehtari, A., Simpson, D., Margossian, C.C., Carpenter, B., Yao, Y., Kennedy, L., Gabry, J., Bürkner, P.C., Modrák, M., 2020. Bayesian workflow. URL: https://arxiv.org/abs/2011.01808, arXiv:2011.01808.

Ghahramani, Z., 2015. Probabilistic machine learning and artificial intelligence. Nature 521, 452–459.

Gruber, C., Schenk, P.O., Schierholz, M., Kreuter, F., Kauermann, G., 2025. Sources of uncertainty in supervised machine learning – a statisticians' view. URL: https://arxiv.org/abs/2305.16703, arXiv:2305.16703.

Homan, M.D., Gelman, A., 2014. The no-u-turn sampler: adaptively setting path lengths in hamiltonian monte carlo. J. Mach. Learn. Res. 15, 1593–1623.

Hu, C., Lee, Z., Franz, B., 2012. Chlorophyll aalgorithms for oligotrophic oceans: A novel approach based on three-band reflectance difference. Journal of Geophysical Research: Oceans 117. doi:https://doi.org/10.1029/2011JC007395.

Jaynes, E., Bretthorst, G., 2003. Probability Theory: The Logic of Science. Cambridge University Press. URL: https://books.google.com/books?id=tTN4HuUNXjgC.

JCGM, 2008. Evaluation of Measurement Data – Guide to the Expression of Uncertainty in Measurement. Technical Report JCGM 100:2008. Joint Committee for Guides in Metrology (JCGM). Sèvres, France. URL: https://www.bipm.org/en/publications/guides/gum.html. gUM 1995 with minor corrections.

McElreath, R., 2020. Statistical Rethinking: A Bayesian Course with Examples in R and Stan. 2 ed., CRC Press.

Nguyen, A.B., Bonici, M., McGee, G., Percival, W.J., 2025. Loo-pit: A sensitive posterior test. Journal of Cosmology and Astroparticle Physics 2025, 008. URL: https://dx.doi.org/10.1088/1475-7516/2025/01/008, doi:10.1088/1475-7516/2025/01/008.

O'Reilly, J.E., Maritorena, S., Mitchell, B.G., Siegel, D.A., Carder, K.L., Garver, S.A., Kahru, M., McClain, C., 1998. Ocean color chlorophyll algorithms for seawifs. Journal of Geophysical Research: Oceans 103, 24937–24953. doi:https://doi.org/10.1029/98JC02160.

O'Reilly, J.E., Werdell, P.J., 2019. Chlorophyll algorithms for ocean color sensors - oc4, oc5 & oc6. Remote Sensing of Environment 229, 32–47. doi:https://doi.org/10.1016/j.rse.2019.04.021.

O'Reilly, J.E., Maritorena, S., Siegel, D.A., O'Brien, M.C., Toole, D., Mitchell, B.G., Kahru, M., Chavez, F.P., Strutton, P., Cota, G.F., et al., 2000. Ocean color chlorophyll a algorithms for seawifs, oc2, and oc4: Version 4. SeaWiFS postlaunch calibration and validation analyses, Part 3, 9–23.

Scheemaekere, X.D., Szafarz, A., 2011. The inference fallacy from bernoulli to kolmogorov. URL: https://www.researchgate.net/publication/254450993_The_Inference_Fallacy_From_Bernoulli_to_Kolmogorov. cEB Working Paper N° 11/006, February 2011.

Seegers, B.N., Stumpf, R.P., Schaeffer, B.A., Loftin, K.A., Werdell, P.J., 2018. Performance metrics for the assessment of satellite data products: an ocean color case study. Opt. Express 26, 7404–7422. doi:10.1364/OE.26.007404.

Shi, Y., Zhou, X., Yang, X., Shi, L., Ma, S., 2015. Merging satellite ocean color data with bayesian maximum entropy method. IEEE Journal of Selected Topics in Applied Earth Observations and Remote Sensing 8, 3294–3304. doi:10.1109/JSTARS.2015.2425691.

Säilynoja, T., Bürkner, P.C., Vehtari, A., 2022. Graphical test for discrete uniformity and its applications in goodness-of-fit evaluation and multiple sample comparison. Statistics and Computing 32. URL: http://dx.doi.org/10.1007/s11222-022-10090-6, doi:10.1007/s11222-022-10090-6.

Tilstone, G., Mélin, F., Jackson, T., Valente, A., Bailey, S., Moore, T., Kahru, M., Boss, E., Mitchell, B.G., Wang, M., Maritorena, S., et al., 2020. Uncertainties in Ocean Colour Remote Sensing. Technical Report Report 18. International Ocean Colour Coordinating Group (IOCCG). Dartmouth, Canada. URL: https://ioccg.org/what-we-do/ioccg-publications/ioccg-report-series/ioccg-report-18/. iOCCG Report Series, 124 pp.

Vehtari, A., Gelman, A., Gabry, J., 2016. Practical bayesian model evaluation using leave-one-out cross-validation and waic. Statistics and Computing 27, 1413–1432. doi:10.1007/s11222-016-9696-4.

Vehtari, A., Simpson, D., Gelman, A., Yao, Y., Gabry, J., 2024. Pareto smoothed importance sampling. URL: https://arxiv.org/abs/1507.02646, arXiv:1507.02646.

Werdell, P., Bailey, S., 2005. An improved bio-optical data set for ocean color algorithm development and satellite data product validation. Remote Sensing of Environment 98, 122–140.

Werther, M., Burggraaff, O., 2023. Dive into the unknown: Embracing uncertainty to advance aquatic remote sensing. Journal of Remote Sensing 3, 0070. doi:10.34133/remotesensing.0070.

Werther, M., Burggraaff, O., Gurlin, D., Saranathan, A.M., Balasubramanian, S.V., Giardino, C., Braga, F., Bresciani, M., Pellegrino, A., Pinardi, M., Simis, S.G.H., Lehmann, M.K., Kangro, K., Alikas, K., Ficek, D., Odermatt, D., 2025. On the generalization ability of probabilistic neural networks for hyperspectral remote sensing of absorption properties across optically complex waters. Remote Sensing of Environment 328, 114820. doi:10.1016/j.rse.2025.114820.

Werther, M., Odermatt, D., Simis, S.G.H., Gurlin, D., Lehmann, M.K., Kutser, T., Gupana, R., Varley, A., Hunter, P.D., Tyler, A.N., Spyrakos, E., 2022. A bayesian approach for remote sensing of chlorophyll-a and associated retrieval uncertainty in oligotrophic and mesotrophic lakes. Remote Sensing of Environment 283, 113295. URL: https://doi.org/10.1016/j.rse.2022.113295, doi:10.1016/j.rse.2022.113295.

Wolkovich, E., Davies, T.J., Pearse, W.D., Betancourt, M., 2024. A four-step bayesian workflow for improving ecological science. URL: https://arxiv.org/abs/2408.02603, arXiv:2408.02603.

Supplementary Material

This supplementary document provides additional model development details, diagnostic plots, and extended results that support the main manuscript. Figures and tables are numbered sequentially as S1, S2, etc., and are referenced in the order they are discussed.

1. Additional Model Structures and Equations

1.1. Model 2: Hierarchical Linear Regression (HLR)

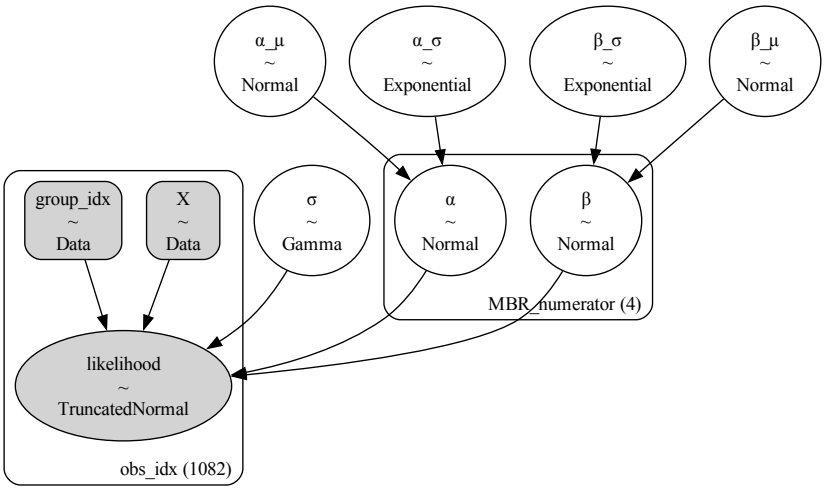

Figure S1: Model 2 Directed Acyclic Graph (DAG). Group-specific intercepts α_g and slopes β_g are modeled hierarchically by MBR numerator group g. Gaussian priors are used for all group-level parameters, with hyperpriors on their means and standard deviations to allow partial pooling. A shared dispersion parameter σ is modeled with a Gamma prior. Observations are modeled via a truncated normal distribution.

The model specification is:

$$\alpha_\mu \sim \mathcal{N}(0, 1), \qquad \alpha_\sigma \sim \text{Exponential}(1), \tag{1}$$

$$\beta_\mu \sim \mathcal{N}(0, 1), \qquad \beta_\sigma \sim \text{Exponential}(1), \tag{2}$$

$$\sigma_\gamma \sim \text{Exponential}(1), \qquad \sigma_\phi \sim \text{Exponential}(1), \tag{3}$$

$$\alpha_g \sim \mathcal{N}(\alpha_\mu, \alpha_\sigma), \qquad \beta_g \sim \mathcal{N}(\beta_\mu, \beta_\sigma), \tag{4}$$

$$\sigma \sim \text{Gamma}(\sigma_\gamma, \sigma_\phi), \tag{5}$$

$$\mu_i = \alpha_{g[i]} + \beta_{g[i]}\, x_i, \tag{6}$$

$$y_i \sim \text{TruncatedNormal}(\mu_i, \sigma, -3, 3.2). \tag{7}$$

1.2. Model 3: HLR with Group-Specific Dispersion

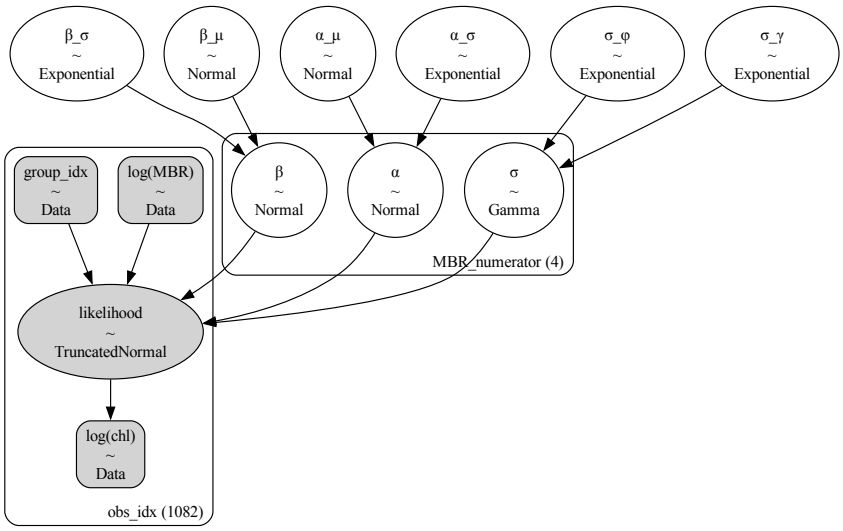

Figure S2: Model 3 DAG. Extends Model 2 by allowing the dispersion parameter σ_g to vary by MBR numerator group, modeled with a Gamma prior for each group.

The model specification is:

$$\alpha_\mu \sim \mathcal{N}(0, 1), \qquad \alpha_\sigma \sim \text{Exponential}(1), \tag{8}$$

$$\beta_\mu \sim \mathcal{N}(0, 1), \qquad \beta_\sigma \sim \text{Exponential}(1), \tag{9}$$

$$\sigma_\gamma \sim \text{Exponential}(1), \qquad \sigma_\phi \sim \text{Exponential}(1), \tag{10}$$

$$\alpha_g \sim \mathcal{N}(\alpha_\mu, \alpha_\sigma), \qquad \beta_g \sim \mathcal{N}(\beta_\mu, \beta_\sigma), \tag{11}$$

$$\sigma_g \sim \text{Gamma}(\sigma_\gamma, \sigma_\phi), \tag{12}$$

$$\mu_i = \alpha_{g[i]} + \beta_{g[i]}\, x_i, \tag{13}$$

$$y_i \sim \text{TruncatedNormal}(\mu_i, \sigma_{g[i]}, -3, 3.2). \tag{14}$$

1.3. Model 4: HLR with Input-Dependent Dispersion

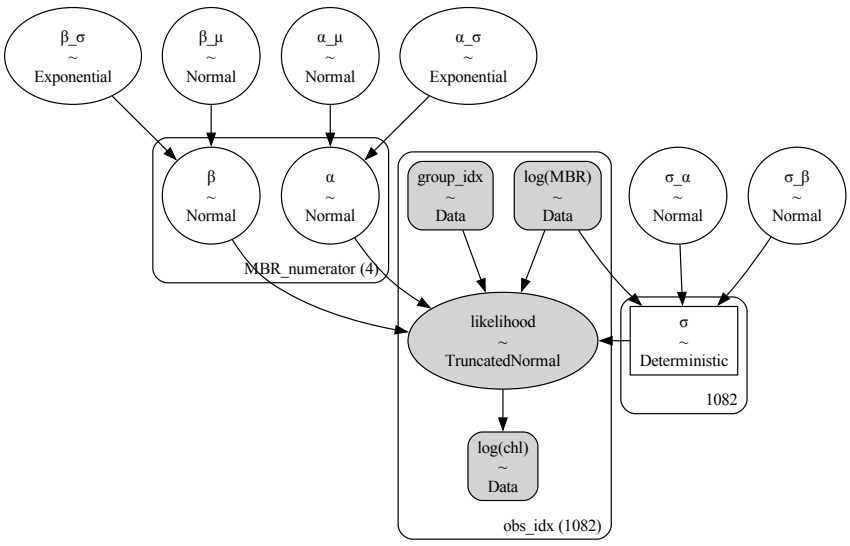

Figure S3: Model 4 DAG. Extends Model 2 by modeling the log-dispersion as a linear function of log(MBR) with shared slope and intercept, allowing variance to change with the predictor.

The model specification is:

$$\alpha_\mu \sim \mathcal{N}(0, 1), \qquad \alpha_\sigma \sim \text{Exponential}(1), \tag{15}$$

$$\beta_\mu \sim \mathcal{N}(0, 1), \qquad \beta_\sigma \sim \text{Exponential}(1), \tag{16}$$

$$\alpha_g \sim \mathcal{N}(\alpha_\mu, \alpha_\sigma), \qquad \beta_g \sim \mathcal{N}(\beta_\mu, \beta_\sigma), \tag{17}$$

$$\sigma_\alpha \sim \mathcal{N}(0, 1), \qquad \sigma_\beta \sim \mathcal{N}(0, 1), \tag{18}$$

$$\mu_i = \alpha_{g[i]} + \beta_{g[i]}\, x_i, \tag{19}$$

$$\log \sigma_i = \sigma_\alpha + \sigma_\beta\, x_i, \tag{20}$$

$$y_i \sim \text{TruncatedNormal}(\mu_i, e^{\log \sigma_i}, -3, 3.2). \tag{21}$$

1.4. Model 5: Heteroskedastic HLR with Group-Specific Dispersion Slopes

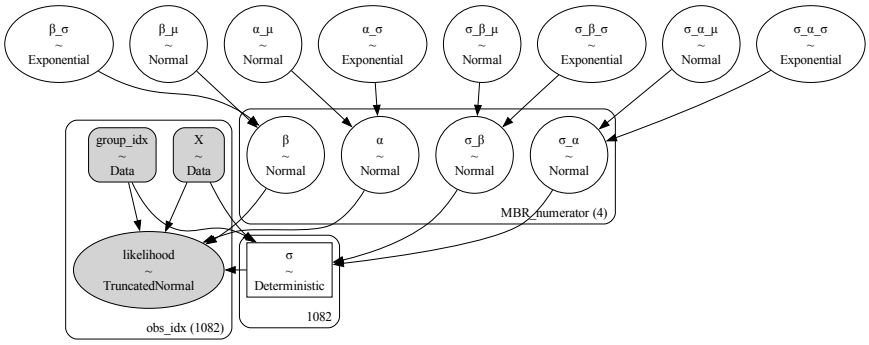

Figure S4: Model 5 DAG. Extends Model 4 by allowing both the intercept and slope of the log-dispersion relationship to vary by MBR numerator group, enabling group-specific heteroskedasticity.

The model specification is:

$$\alpha_\mu \sim \mathcal{N}(0,1), \qquad \alpha_\sigma \sim \text{Exponential}(1), \tag{22}$$
$$\beta_\mu \sim \mathcal{N}(0,1), \qquad \beta_\sigma \sim \text{Exponential}(1), \tag{23}$$
$$\sigma_\alpha^\mu \sim \mathcal{N}(0,1), \qquad \sigma_\alpha^\sigma \sim \text{Exponential}(1), \tag{24}$$
$$\sigma_\beta^\mu \sim \mathcal{N}(0,1), \qquad \sigma_\beta^\sigma \sim \text{Exponential}(1), \tag{25}$$
$$\alpha_g \sim \mathcal{N}(\alpha_\mu, \alpha_\sigma), \qquad \beta_g \sim \mathcal{N}(\beta_\mu, \beta_\sigma), \tag{26}$$
$$\sigma_{\alpha,g} \sim \mathcal{N}(\sigma_\alpha^\mu, \sigma_\alpha^\sigma), \qquad \sigma_{\beta,g} \sim \mathcal{N}(\sigma_\beta^\mu, \sigma_\beta^\sigma), \tag{27}$$
$$\mu_i = \alpha_{g[i]} + \beta_{g[i]}\, x_i, \tag{28}$$
$$\log \sigma_i = \sigma_{\alpha,g[i]} + \sigma_{\beta,g[i]}\, x_i, \tag{29}$$
$$y_i \sim \text{TruncatedNormal}(\mu_i, e^{\log \sigma_i}, -3, 3.2). \tag{30}$$

2. Posterior Diagnostics: Trace plots and Forest Plots

This section presents Markov chain Monte Carlo (MCMC) diagnostics for all five models. For each model, I show:

1. **Trace plots** for all parameters, displaying individual chain trajectories and combined posterior densities. Well-mixed, stationary chains with substantial overlap between chains indicate stable sampling.
2. **Forest plots** for most model parameters, displaying posterior distributions (central tendency and dispersion), effective sample sizes (ESS), and Gelman–Rubin convergence diagnostics ($\hat{R}$). For Models 4 and 5, dispersion parameters σ_i are excluded due to their being observation-specific.

2.1. Trace Plots

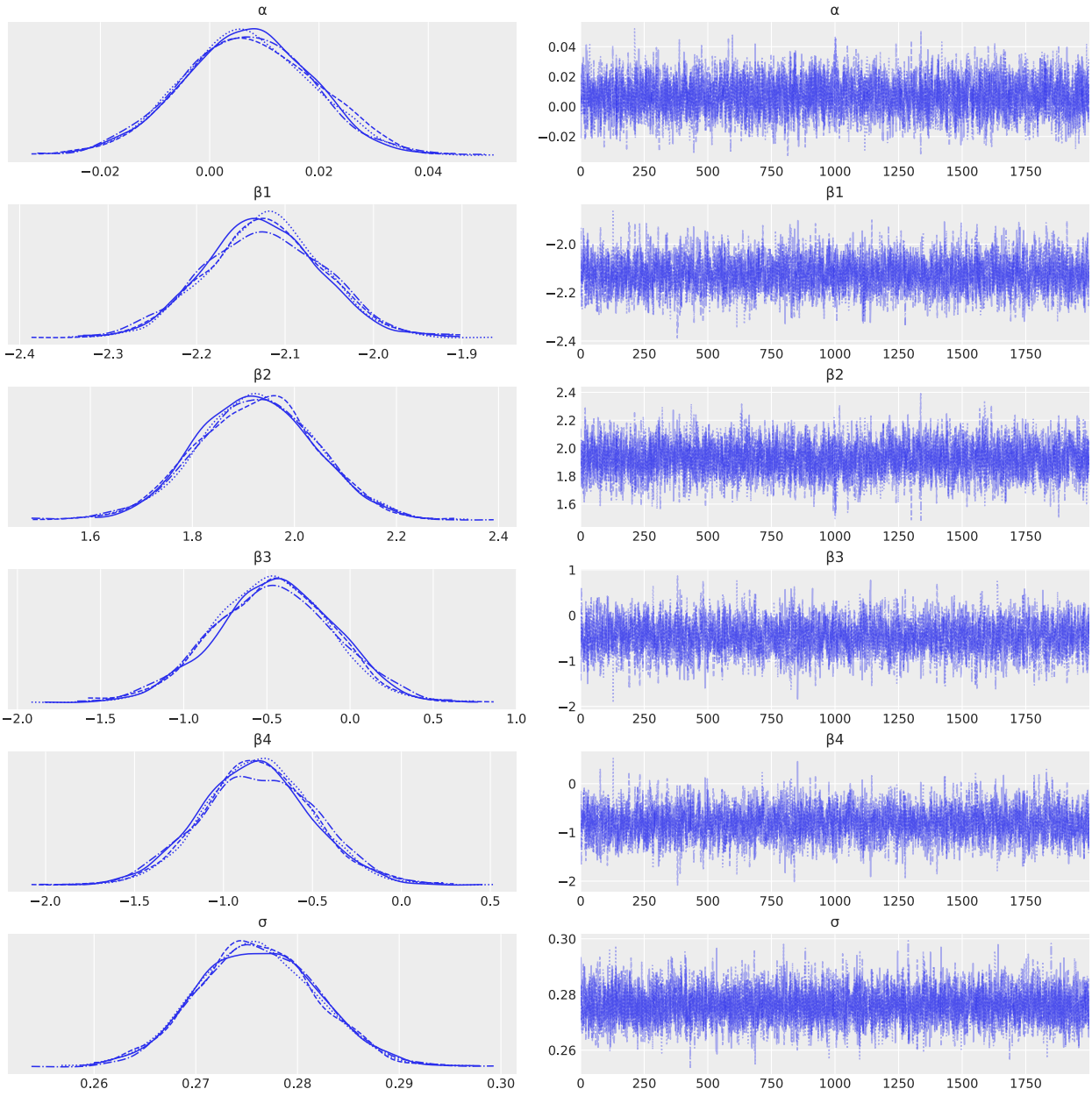

Figure S5: Traceplots for **Model 1** showing MCMC sampling behavior for all parameters. Left sub-panels show the parameter posterior densities. Right corresponding sub-panels display chain trajectories; well-mixed and stationary patterns with substantial overlap across chains indicate stable sampling and good convergence.

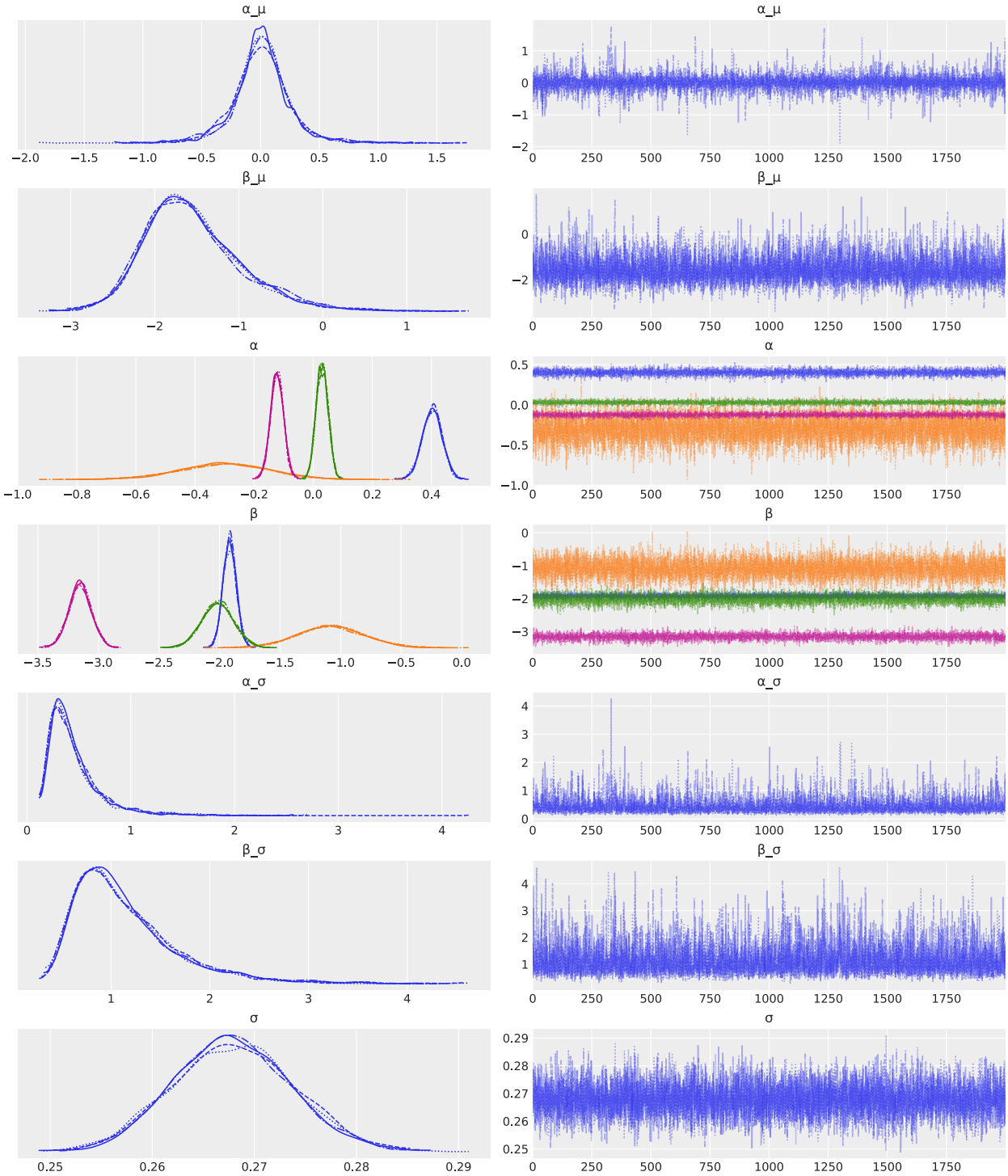

Figure S6: Traceplots for **Model 2** showing MCMC sampling behavior for all parameters, including group-indexed effects where applicable. Sub-panels show parameter posterior densities. Right sub-panels display chain trajectories; well-mixed and stationary patterns with substantial overlap across chains indicate stable sampling and good convergence. For hierarchical parameters, separate chains are shown for each group-level effect, allowing visual assessment of convergence across all levels.

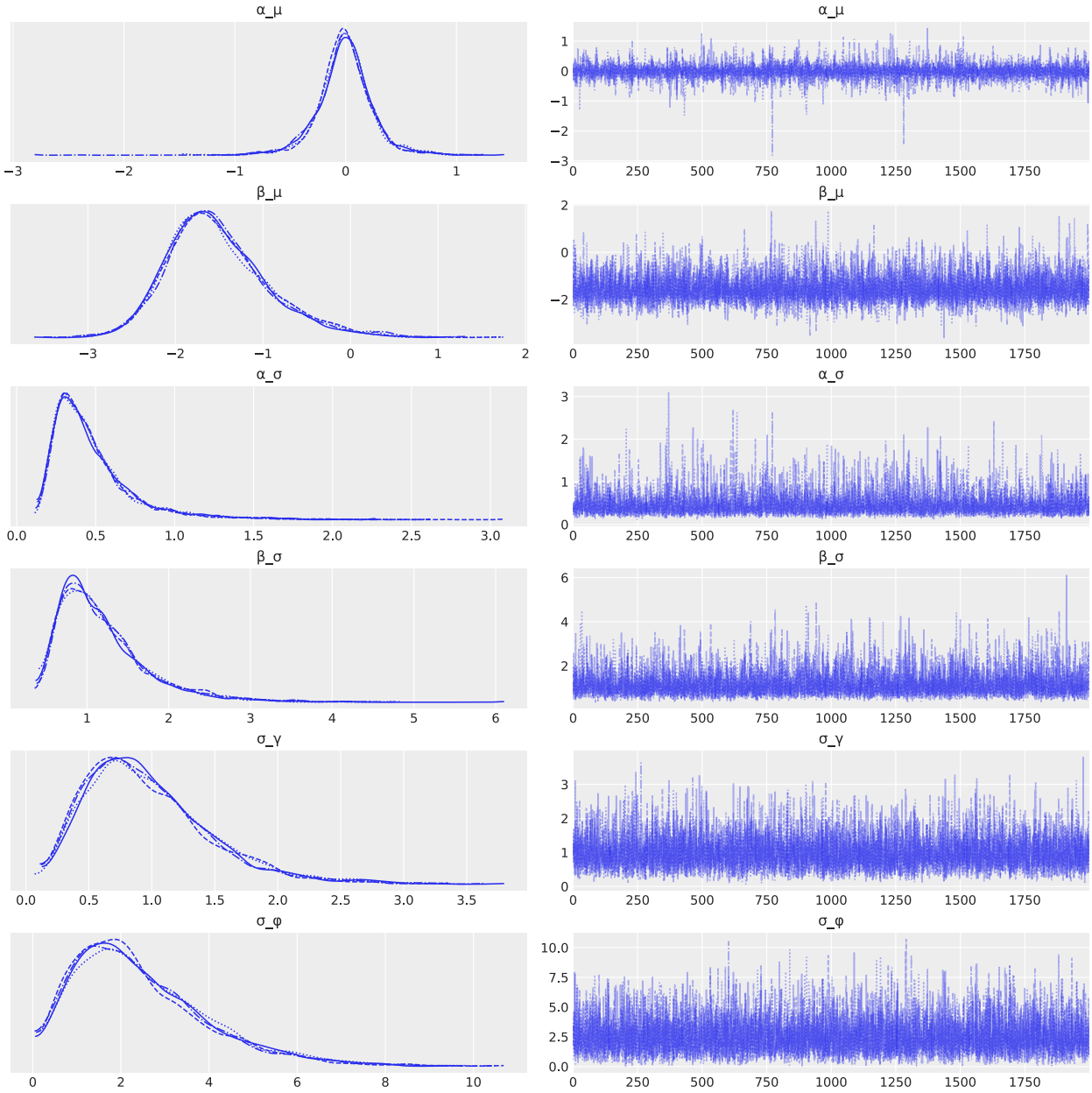

Figure S7: Traceplots for **Model 3** (Part 1 of 2): *hyperparameters*. Posterior densities (left) and MCMC chains (right) for hyperparameters governing the group-indexed mean parameters, $(\alpha_\mu, \alpha_\sigma, \beta_\mu, \beta_\sigma)$, and for the dispersion hyperparameters $(\sigma_\gamma, \sigma_\phi)$. Chains exhibit stable mixing and convergence across all hyperparameters.

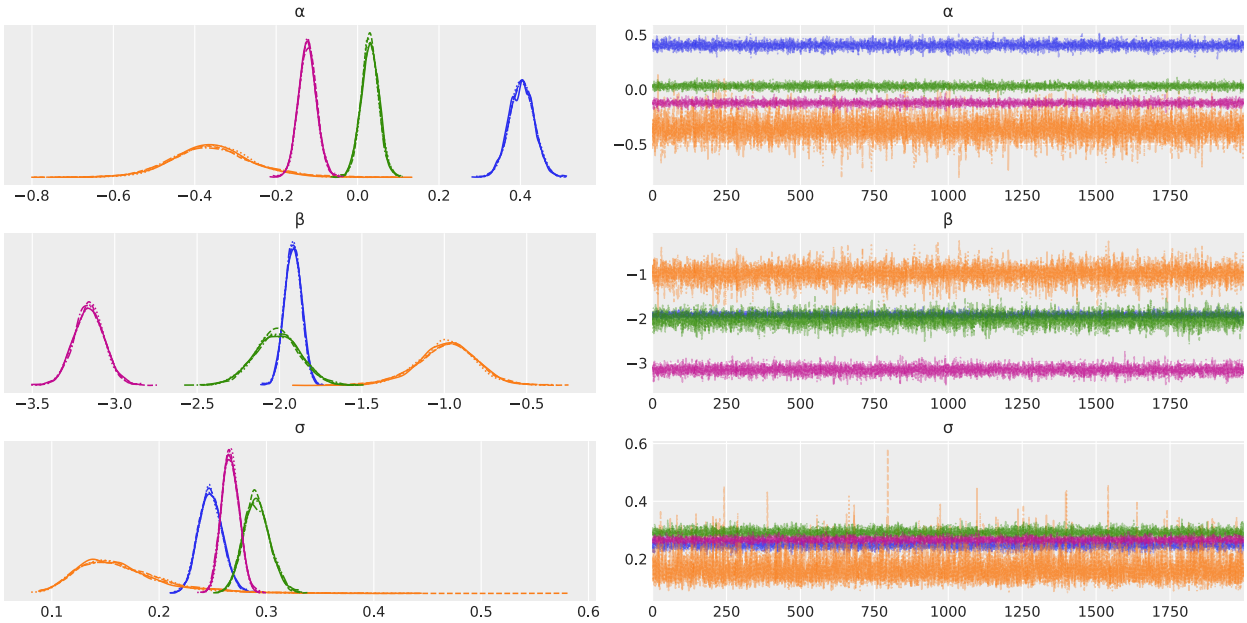

Figure S8: Traceplots for **Model 3** (Part 2 of 2): *group-level parameters*. Posterior densities (left) and MCMC chains (right) for α (vector of group-indexed intercepts), β (vector of group-indexed slopes), and σ (vector of group-indexed dispersions). Colors distinguish MBR numerator groups for vector-valued parameters; the mapping is omitted as the traceplots are intended for diagnosing mixing and convergence rather than comparing magnitudes (see forest plots for inter-group comparisons).

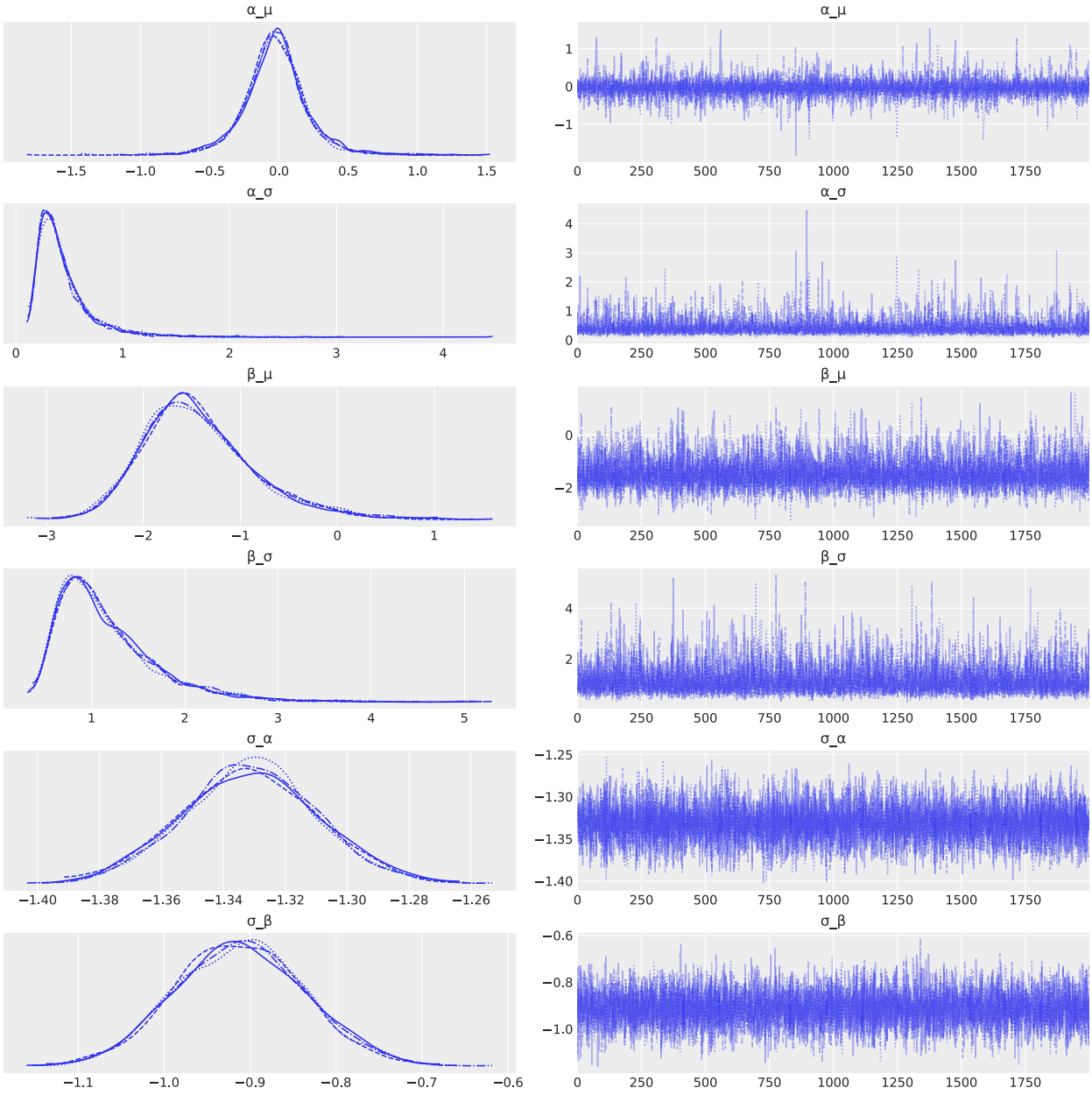

Figure S9: Traceplots for **Model 4** (Part 1 of 2): *hyperparameters and global variance-function coefficients*. Panels show posterior densities (left column) and MCMC chain trajectories (right column) for hyperparameters governing the group-level intercepts and slopes $(\alpha_\mu, \alpha_\sigma, \beta_\mu, \beta_\sigma)$, together with the global variance-function coefficients $(\sigma_\alpha, \sigma_\beta)$ from $\log \sigma_i = \sigma_\alpha + \sigma_\beta \log(\mathrm{MBR}_i)$.

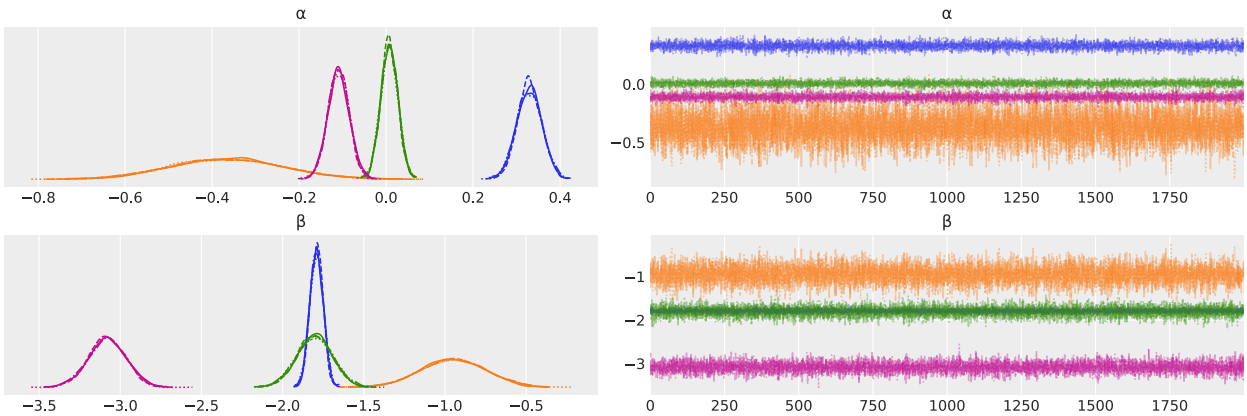

Figure S9: Traceplots for **Model 4** (Part 2 of 2): *group-level mean parameters*. Posterior densities (left) and MCMC chains (right) are shown for group-indexed intercepts and slopes (α, β) by MBR numerator group. Colors denote groups; per-panel color–group mapping is not shown since the purpose is to diagnose mixing and convergence rather than to compare group magnitudes.

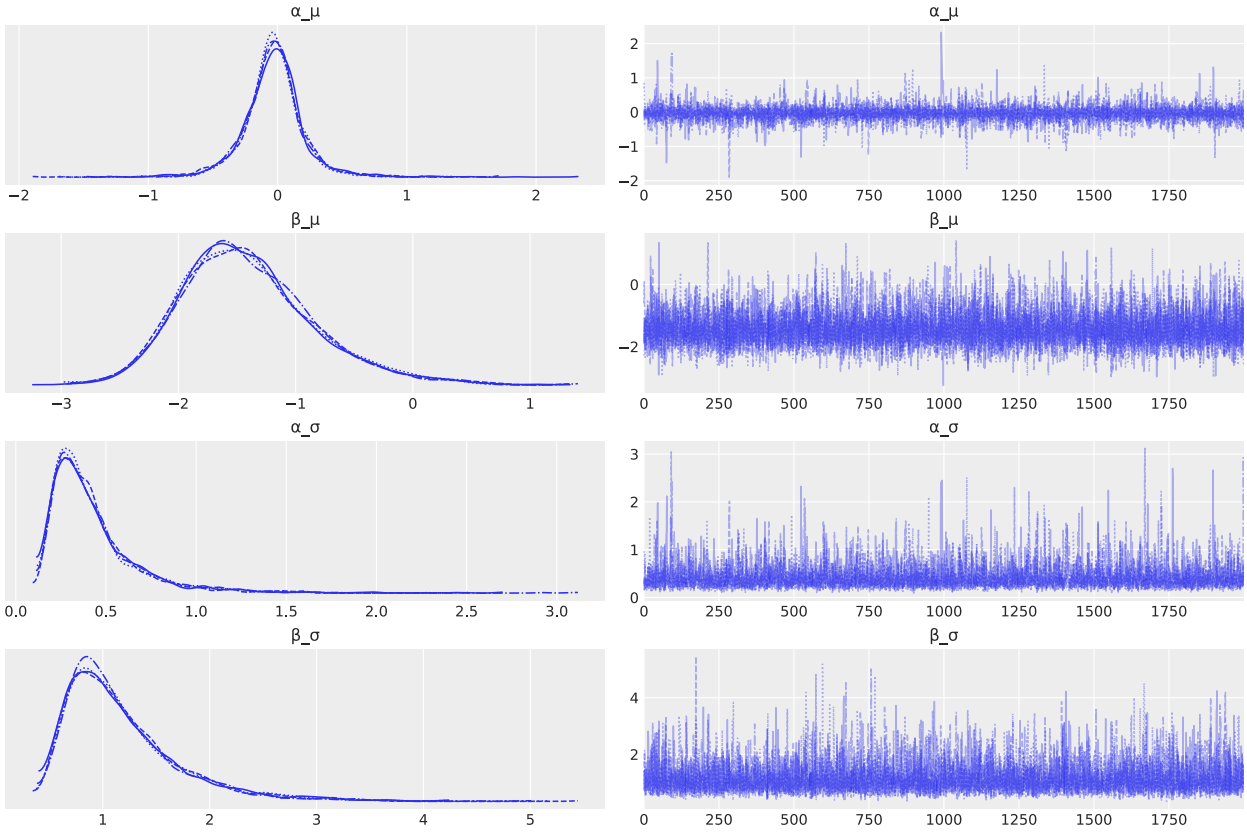

Figure S10: Traceplots for **Model 5** (Part 1 of 3): *hyperparameters for group-indexed mean parameters.* Posterior densities (left) and MCMC chains (right) for $(\alpha_\mu, \alpha_\sigma, \beta_\mu, \beta_\sigma)$, which govern the vectors α (group-indexed intercepts) and β (group-indexed slopes). Colors within vector-valued panels correspond to MBR numerator groups; the mapping is omitted because these plots are for mixing/convergence diagnostics (see forest plots for inter-group comparisons).

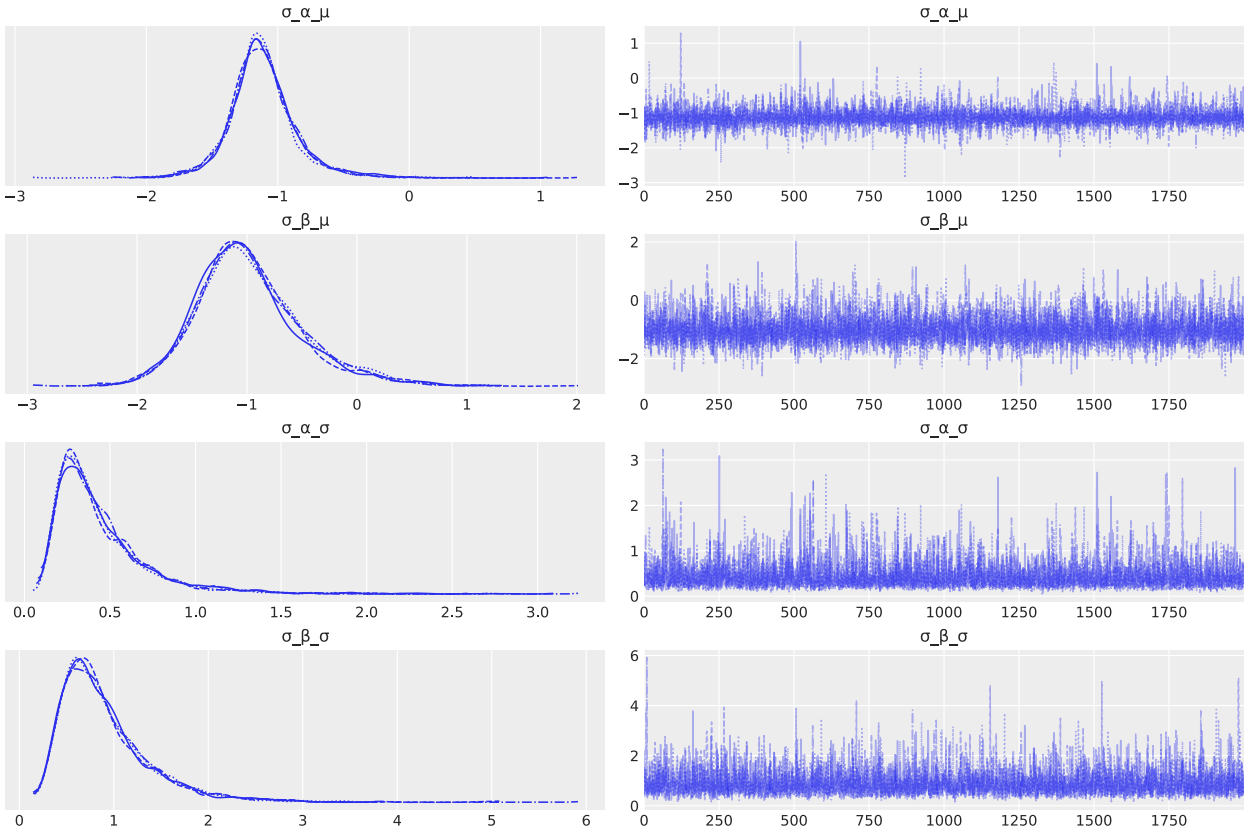

Figure S10: Traceplots for **Model 5** (Part 2 of 3): *hyperparameters for group-indexed variance-function parameters*. Posterior densities (left) and chains (right) for $(\sigma_\alpha^\mu, \sigma_\alpha^\sigma, \sigma_\beta^\mu, \sigma_\beta^\sigma)$, which govern the vectors σ_α and σ_β; *cf.* S10 part 3.

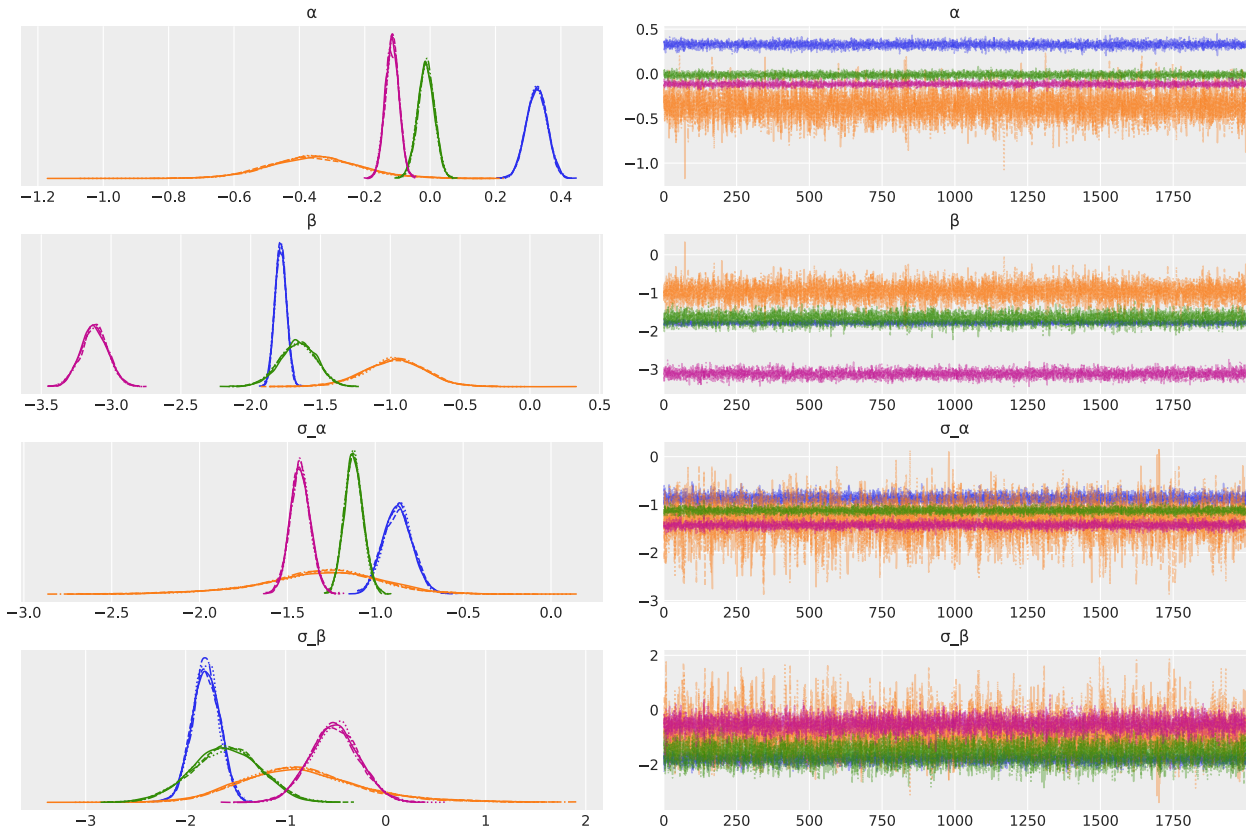

Figure S10: Traceplots for **Model 5** (Part 3 of 3): *group-indexed parameters*. Colors denote MBR numerator groups for vector-valued parameters. Posterior densities (left) and chains (right) for α (vector of group-indexed intercepts), β (vector of group-indexed slopes), and the variance-function vectors σ_α and σ_β (one intercept and slope per MBR numerator group) in $\log \sigma[\text{group}_i] = \sigma_\alpha[\text{group}_i] + \sigma_\beta[\text{group}_i] \log(\text{MBR}[\text{group}_i])$. This yields observations specific σ_j; not shown to maintain clarity, as including hundreds of traces would obscure the primary diagnostics without improving convergence assessment.

2.2. Forest Plots

In the forest plots, the left panel shows each parameter's posterior distribution with median (point) and highest density interval (whiskers). Note that for clarity only first-level parameters are shown, not their hyperparameters. Moreover, Model 4 and 5 have σ posteriors for each observation, and these are omitted from all plots, again for clarity. The middle panel displays the bulk ESS for each depicted parameter; values well above 1000 indicate stable estimation despite potential autocorrelation in chains. The right panel shows $\hat{R}$ values, with values close to 1.00 indicating convergence across chains.

Some posterior distributions have intervals overlapping zero. In a Bayesian context, this means that the posterior includes both positive and negative values with non-negligible probability, and thus the direction of the effect is not strongly supported by the data under the current model and priors.

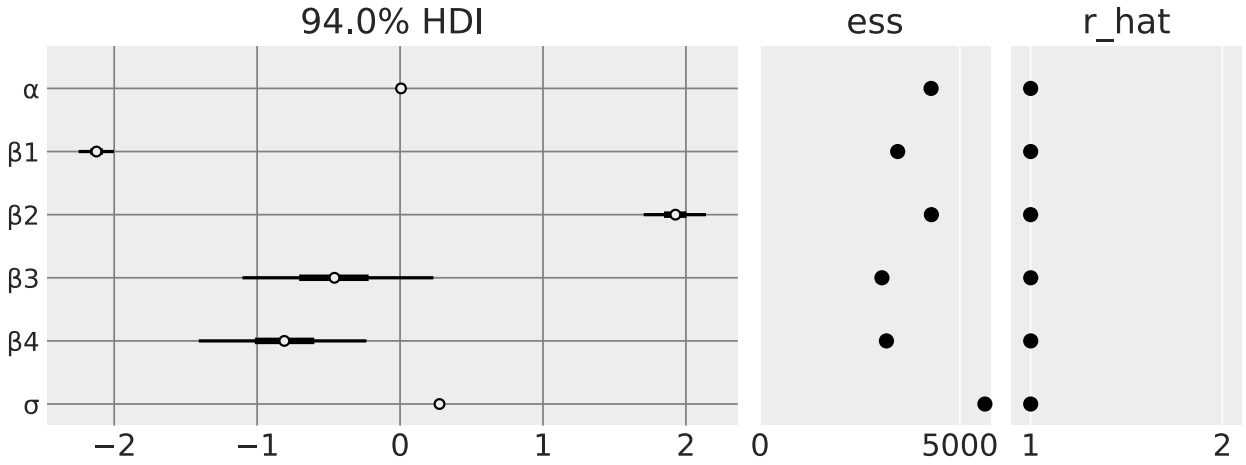

Figure S11: Forest plots of posterior distributions for Model 1. Central dots indicate posterior medians, thick bars show the inter-quartile range (25th–75th percentiles), and thin bars denote the 94% highest density interval (HDI). Effective sample sizes (ESS) and $\hat{R}$ convergence diagnostics are shown in adjacent panels, confirming robust sampling performance.

Interpretation Notes for Forest Plots

- **Relative CI length (all parameters)**: Shorter CIs imply greater certainty in the parameter estimate; longer CIs signal less information in the data about that parameter or stronger regularization from the prior.
- **Intercepts (α_g)**: If a group's credible interval (CI) overlaps zero, this indicates that the baseline log(Chl) for that group could plausibly be near $10^0 = 1$ mg m^{-3}. .
- **Slopes (β_g)**: If a slope's CI overlaps zero, the model cannot rule out the possibility of no linear relationship between log(MBR) and log(Chl) for that group. Wide overlap suggests high uncertainty in how strongly MBR explains chlorophyll variability in that group.
- **Shared σ**: For models with a common dispersion parameter, the CI length reflects uncertainty in the overall noise level. Narrow intervals imply more confidence in the model's estimate of residual variance.

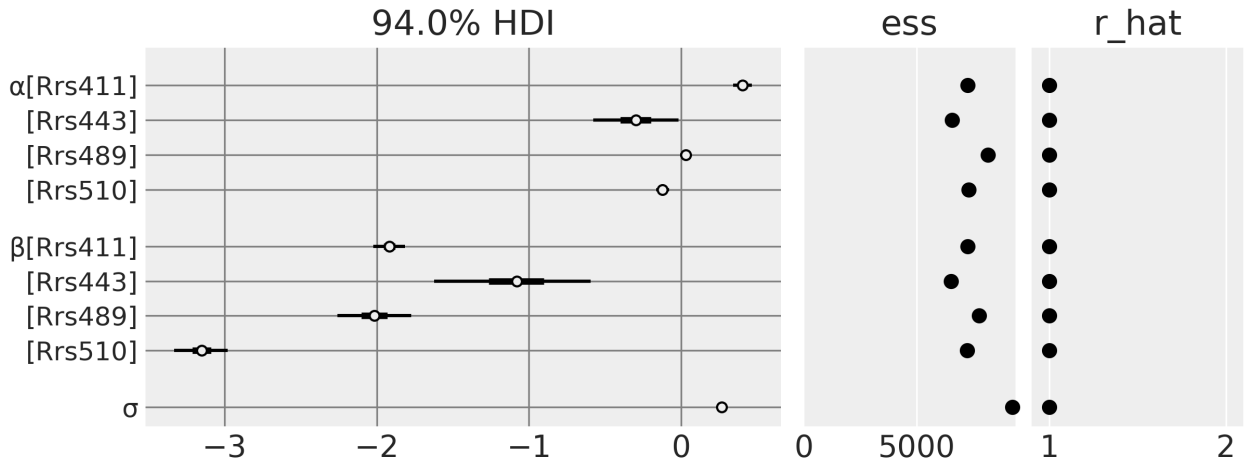

Figure S12: Forest plot for **Model 2**. Group-indexed parameters α (intercepts) and β (slopes) have one value per MBR numerator group. The shared dispersion parameter σ is shown on a single row. Posterior intervals overlapping zero indicate weakly informed parameters. ESS and $\hat{R}$ values confirm adequate sampling and convergence.

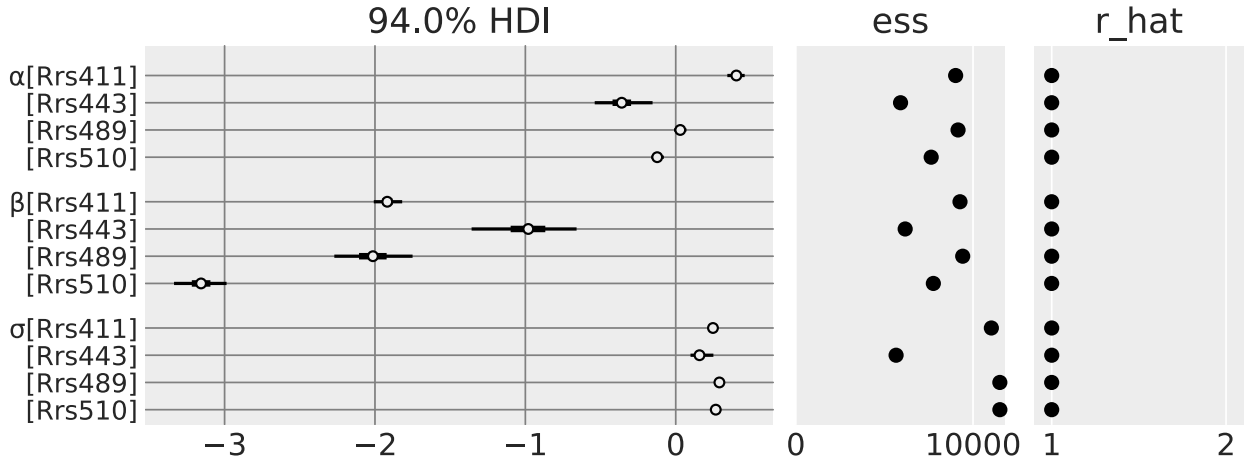

Figure S13: Forest plot for **Model 3**. Three-panel layout (posterior intervals, ESS, $\hat{R}$) for hyperparameters $(\alpha_\mu, \beta_\mu, \alpha_\sigma, \beta_\sigma, \sigma_\gamma, \sigma_\phi)$ and group-indexed parameters (α, β, σ). Group-indexed vectors show one value per MBR numerator group, with colors distinguishing groups. Posterior intervals overlapping zero again indicate limited information for some coefficients, while ESS and $\hat{R}$ panels show good effective sample size and convergence.

- **Group-specific** σ_g: When dispersion varies by group, comparing posterior medians shows which groups exhibit greater residual variability. CI length indicates uncertainty about each group's noise level, and differences in overlap reveal whether groups can be meaningfully distinguished in terms of variance.

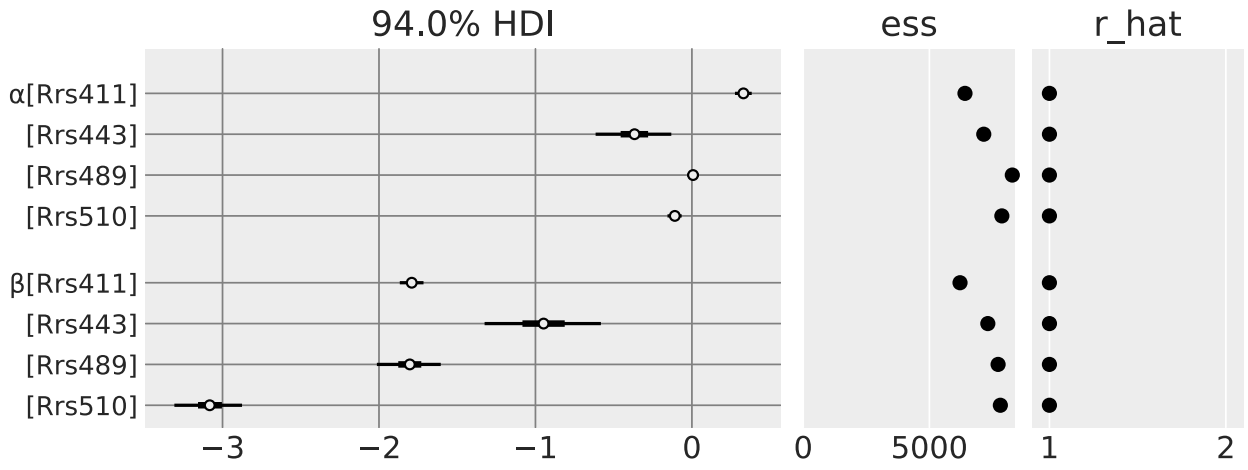

Figure S14: Forest plot for **Model 4**. Panels show posterior intervals (left), ESS (middle), and $\hat{R}$ (right) for group-indexed parameters (α, β), their hyperparameters $(\alpha_\mu, \beta_\mu, \alpha_\sigma, \beta_\sigma)$, and the global variance-function coefficients $(\sigma_\alpha, \sigma_\beta)$. Observation-specific dispersions σ_i are not included, since plotting hundreds of rows would obscure interpretation. Colors indicate MBR numerator groups for vector-valued parameters. ESS and $\hat{R}$ values indicate good mixing and convergence.

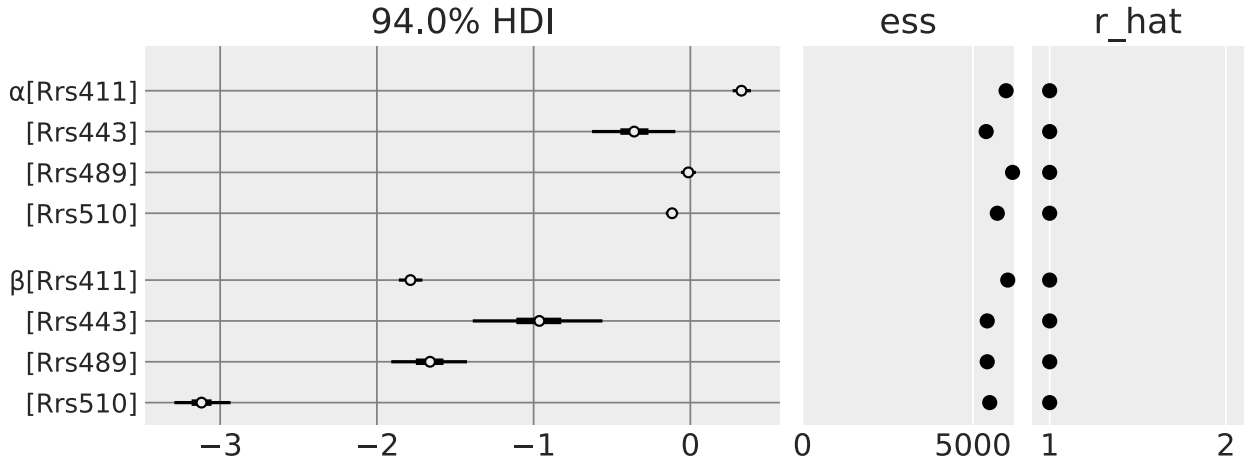

Figure S15: Forest plot for **Model 5**. Three-panel layout (posterior intervals, ESS, $\hat{R}$) for group-indexed mean parameters (α, β), variance-function parameters $(\sigma_\alpha, \sigma_\beta)$, and their hyperparameters. Each vector has one entry per MBR numerator group; colors distinguish groups but the mapping is omitted since the forest plot focuses on magnitude and uncertainty. Observation-specific dispersions σ_i are excluded for clarity. Posterior intervals, ESS, and $\hat{R}$ values confirm stable estimation and convergence across all group- and hyper-level parameters.

Overall, all models exhibit good convergence and adequate sampling efficiency: ESS values are consistently high, and $\hat{R}$ values are effectively 1.00-1.01 for all monitored parameters.

3. In- and Out-of-Sample Performance Assessment

3.1. Predictive Checks and Calibration Plots

This section presents four-panel diagnostic figures for each model. Top row shows prior and posterior predictive checks, providing insight into how well the model has learned from training data. Bottom row shows Leave-One-Out-Probability Integral Transform (LOO-PIT) diagnostics to assess model calibration and potential underdispersion, overdispersion or bias problems on future data. Comparing these plots between models helps understand areas of improvements, as well as identifying potential problems left to resolve.

How to Read LOO-PIT Plots

Calibration target: If the model is well-calibrated, PIT values follow a Uniform$(0, 1)$. Density plots should be flat at 1, and ECDF–uniform difference plots should lie around 0.

Dispersion cues:

- *Hump in the center ($\sim$0.5):* predictive intervals too wide (**over-dispersed**).
- *U-shape (peaks near 0 and 1):* predictive intervals too narrow (**under-dispersed**).

Bias cues:

- *More mass near 1 / ECDF curve below 0:* model **underpredicts** (observed values larger than predicted).
- *More mass near 0 / ECDF curve above 0:* model **overpredicts** (observed values smaller than predicted).

Relation between panels:

- Where PIT density > 1, the ECDF curve slopes upward.
- Where PIT density < 1, the ECDF curve slopes downward.

Together, the two views show both **dispersion** (interval width) and **bias direction** (systematic under- vs. overprediction).

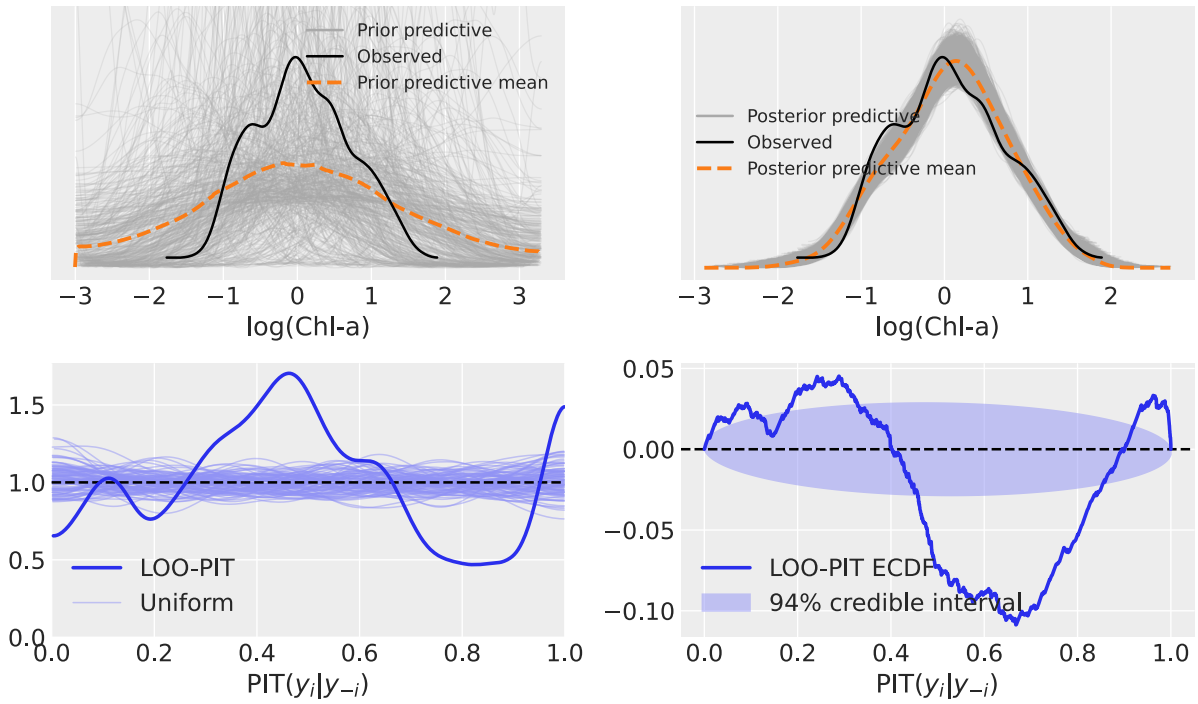

Figure S16: Model 1 4-panel diagnostics. **Top-left:** prior predictive check; observed density (black) shown for visual comparison against prior predictive draws (gray) and their mean (orange dashed). **Top-right:** posterior predictive check; observed log(Chl) density (black) overlaid with posterior predictive draws (gray) and their mean (orange dashed). **Bottom-left:** LOO-PIT kernel density estimate (KDE) in black, with reference KDEs from $\mathcal{U}(0,1)$ draws in light blue; a dashed horizontal line at $y = 1$ indicates ideal calibration. The LOO-PIT density plot departs from uniformity, with noticeable deviations around mid-quantiles, suggesting systematic under- or over-prediction in those regions.**Bottom-right:** LOO-PIT deviance from uniform empirical cumulative distribution function (ECDF) plot; the curve shows the ECDF difference relative to the identity line with a shaded 94% reference envelope under uniformity and a dashed $y = 0$ reference.

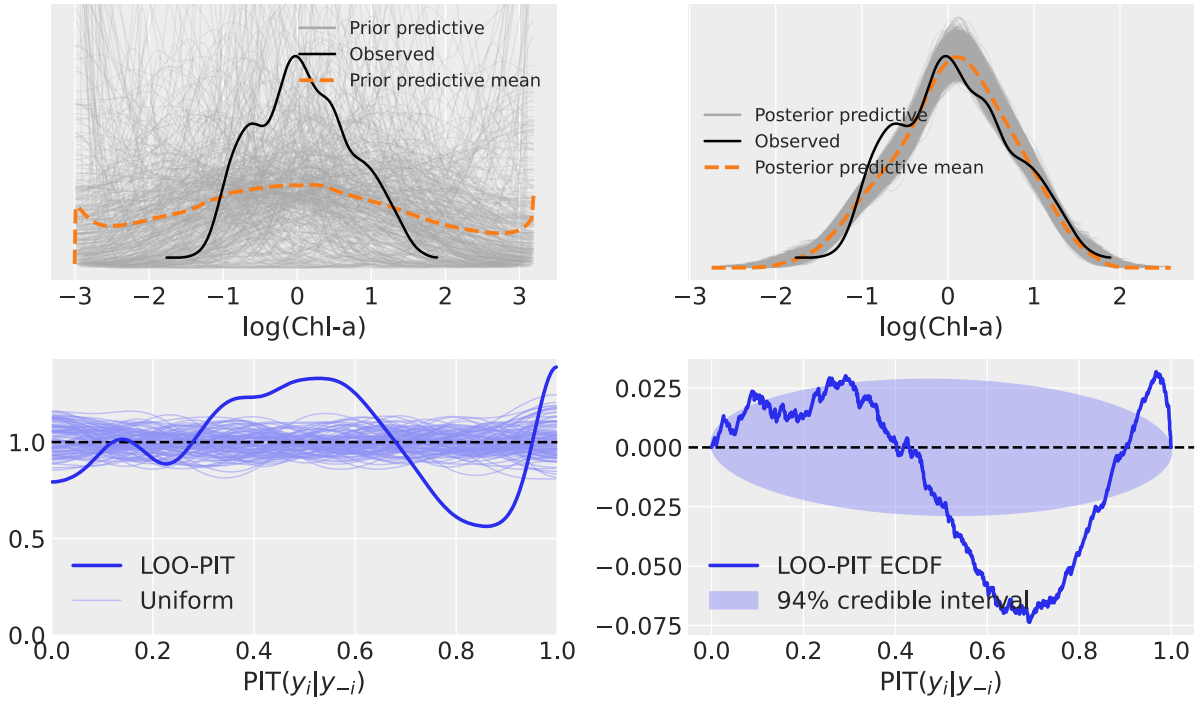

Figure S17: Model 2 - Posterior predictive checks show a closer alignment between predictive mean and observed distribution then with Model 1, particularly in the central region. LOO-PIT diagnostics also improve: the density more closely approximates uniformity, and the ECDF difference plot exhibits smaller deviations within the 94% credible interval. These improvements reflect the benefits of partial pooling across MBR groups, which reduces systematic miscalibration observed in Model 1.

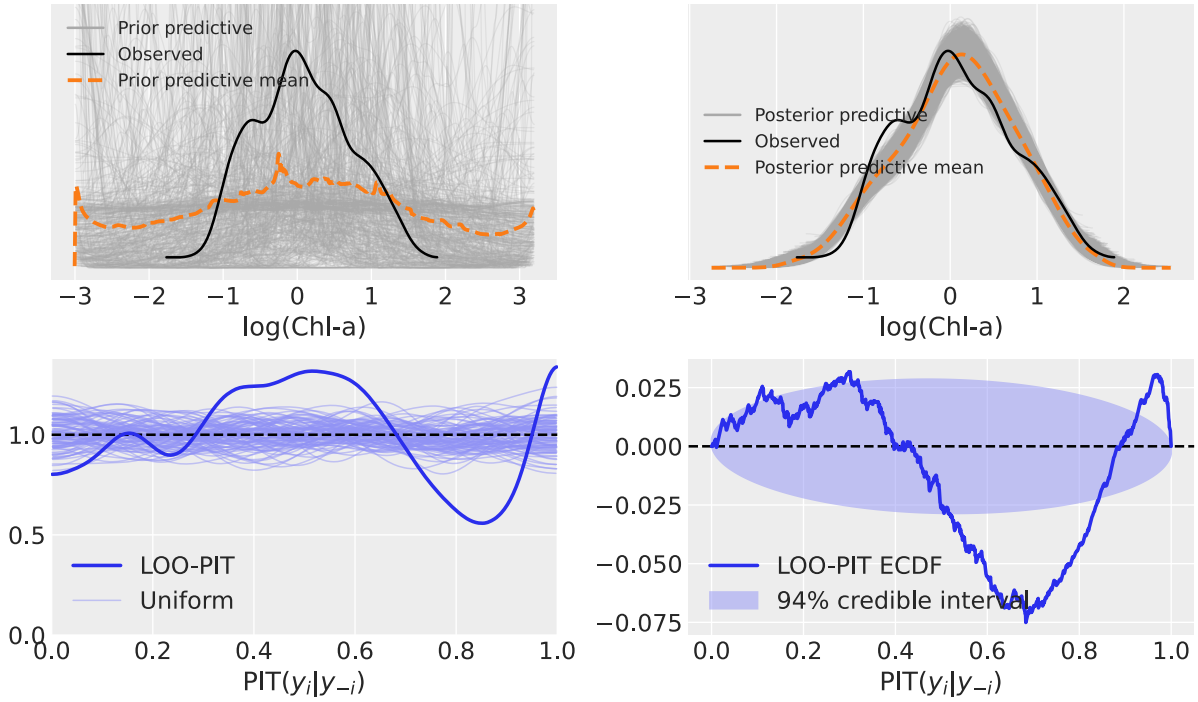

Figure S18: Model 3 - Posterior predictive checks remain well aligned with the observed distribution, with slightly improved representation of the tails. LOO-PIT diagnostics show further gains: the density curve is closer to uniform, and deviations in the ECDF difference plot are reduced in magnitude relative to Model 2. These improvements reflect the introduction of group-specific dispersion, which allows the model to better capture heterogeneity in variance across MBR numerator groups.

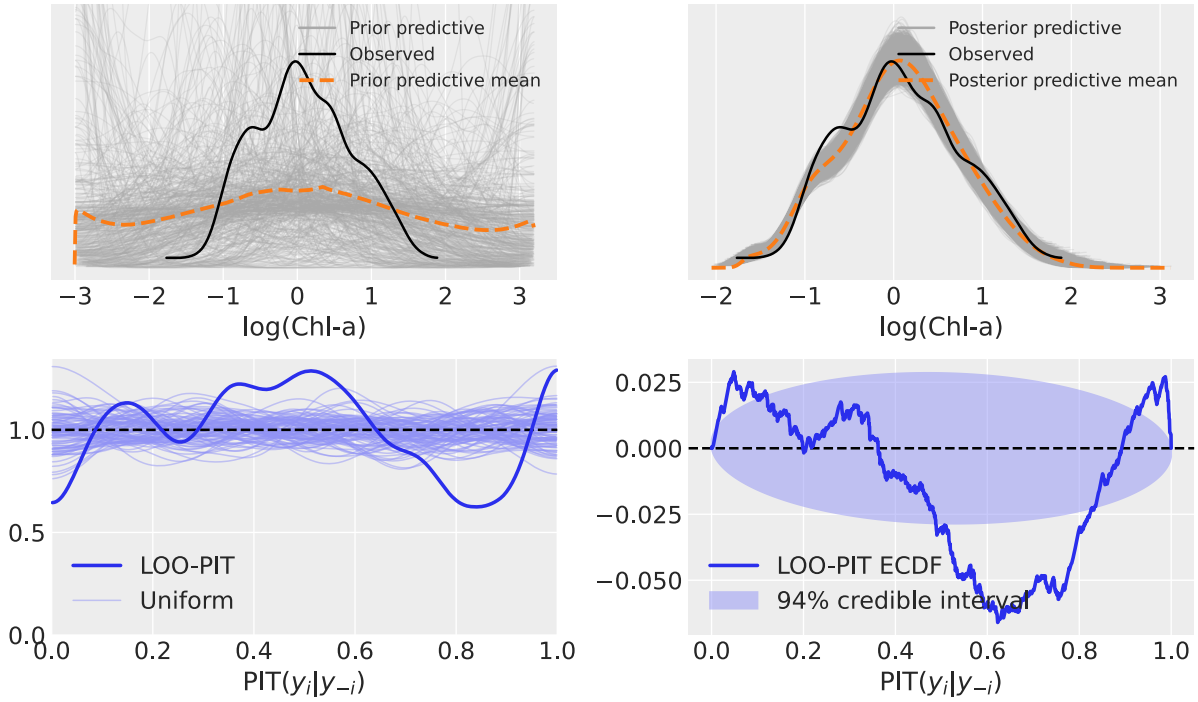

Figure S19: Model 4 - Posterior predictive checks continue to align well with the observed distribution, with modest further improvement in the fit of the tails. LOO-PIT diagnostics show that calibration remains strong: the density curve is smoother and closer to uniform than in Model 3, and the ECDF difference plot shows reduced systematic deviations across mid-quantiles. These gains arise from modeling dispersion as a function of the predictor, which allows the model to better capture input-dependent heteroskedasticity.

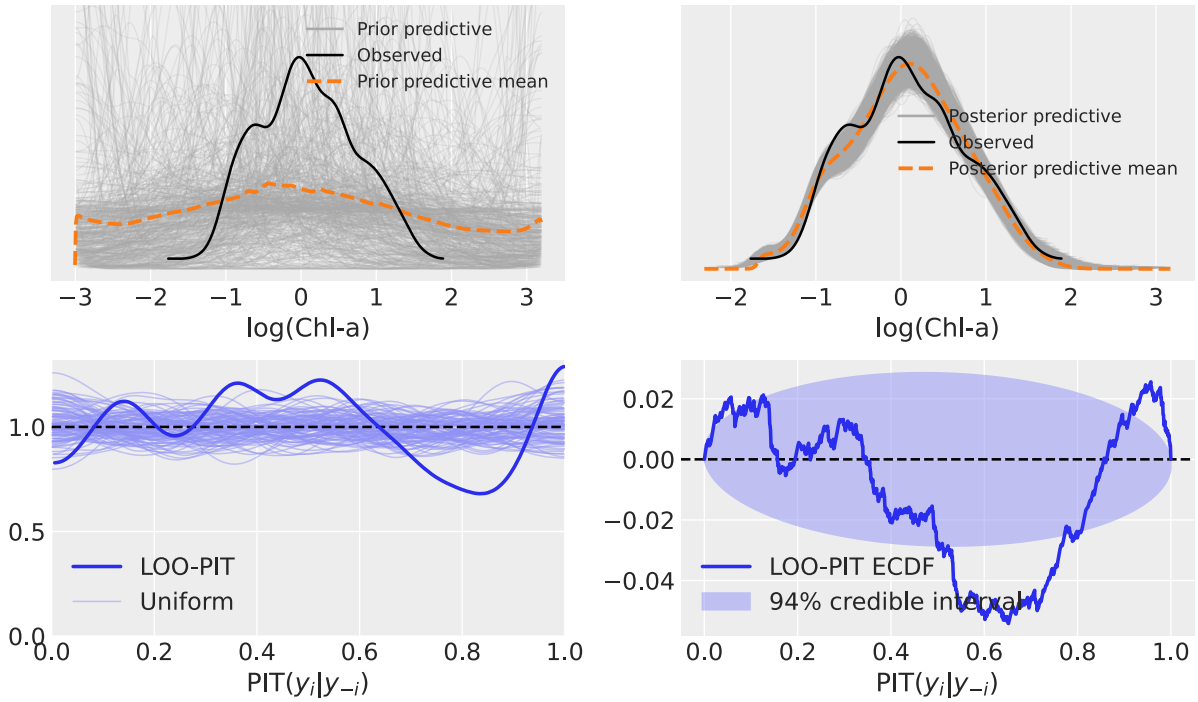

Figure S20: Model 5 - Posterior predictive distributions remain well aligned with observations, with slightly better fit in the distribution tails. The LOO-PIT diagnostics show further calibration gains: the density curve stays closer to uniform across quantiles, and the ECDF difference plot shows narrower deviations well within the 94% credible interval. These improvements stem from allowing both the intercept and slope of the log-dispersion to vary by MBR numerator group, enabling the model to flexibly capture group-specific heteroskedasticity.

3.2. Predictive Coverage Plots

Predictive coverage plots illustrate the proportion of observed chlorophyll-*a* concentrations that fall within the 94% highest density intervals (HDI) of the posterior predictive distribution. These plots provide a visual diagnostic of calibration: ideally, the fraction of covered observations should be close to the nominal level (94%), and deviations highlight under- or over-coverage.

In the predictive coverage plots, the shaded ribbon represents the 94% HDI of the posterior predictive distribution. At any given value of log(MBR) on the x-axis, the ribbon spans vertically along the y-axis to indicate the range within which there is a 94% probability that the predicted log(Chl) lies, conditioned on the data and the model. This direct probabilistic interpretation distinguishes Bayesian predictive intervals from classical confidence intervals, which do not provide probability statements about parameters or predictions.

Figures S21–S25 show predictive coverage for Models 1 through 5, stratified by maximum band ratio (MBR) numerator group. Each panel compares observed values against predictive intervals; black points denote observed log-chlorophyll, shaded bands indicate the posterior predictive HDI, and coverage percentages are summarized in the figure.

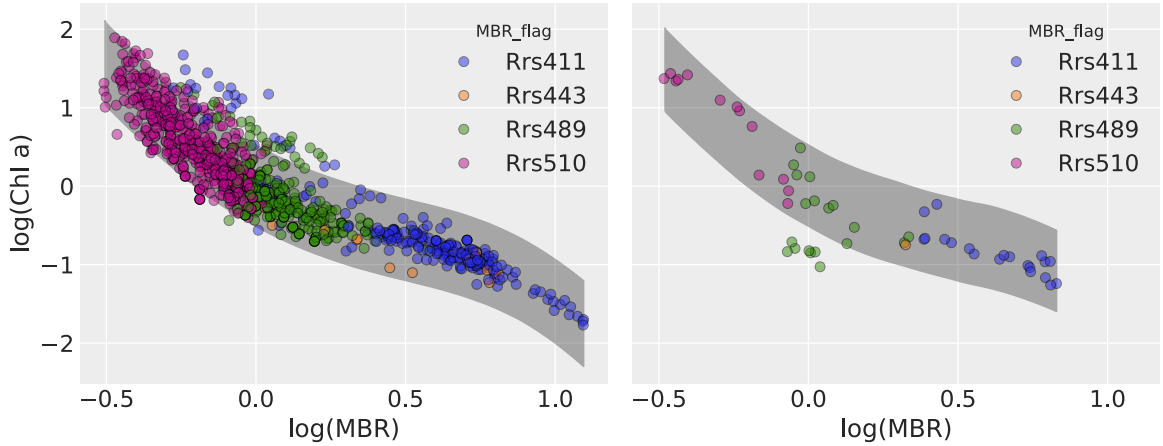

Figure S21: Model 1 predictive coverage. Left: in-sample (NOMAD). Right: out-of-sample (SeaBASS). Gray ribbons show the 94% posterior predictive HDI. In-sample, most MBR numerator groups include observations lying outside the HDI, with the exception of the Rrs443 group (which also has relatively few points). Out-of-sample, a cluster of Rrs489 points falls below the HDI, indicating underestimation of chlorophyll; this miscoverage is consistent with the absence of comparable data in the training range, potentially reflecting a structural limitation of the global polynomial fit.

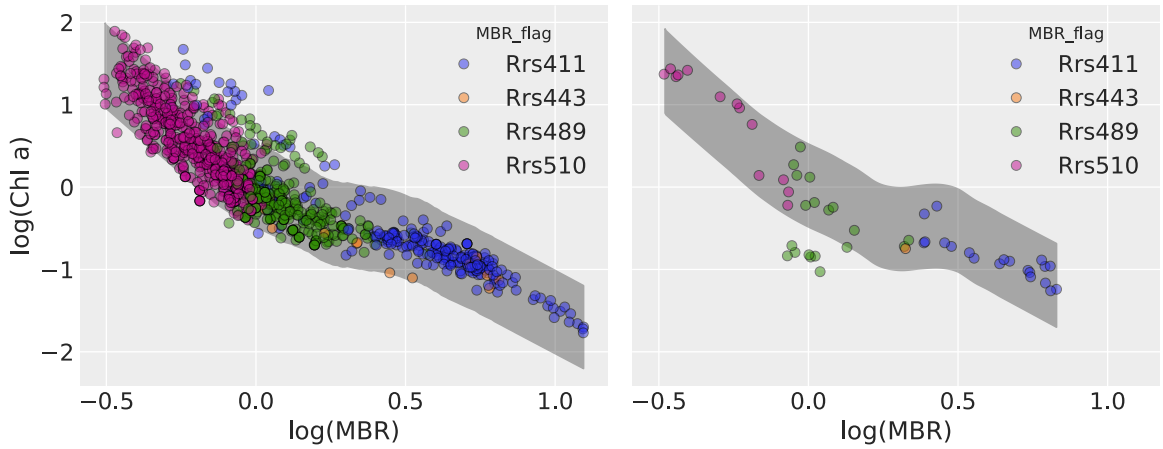

Figure S22: Model 2 predictive coverage. Left: in-sample (NOMAD). Right: out-of-sample (SeaBASS). Gray ribbons show the 94% posterior predictive HDI. The intervals are stratified by MBR numerator group, producing segmented bands that are narrower due to hierarchical shrinkage. In-sample, coverage better follows the tendencies of each group, while out-of-sample the Rrs489 cluster remains outside the HDI but coverage for other groups improves.

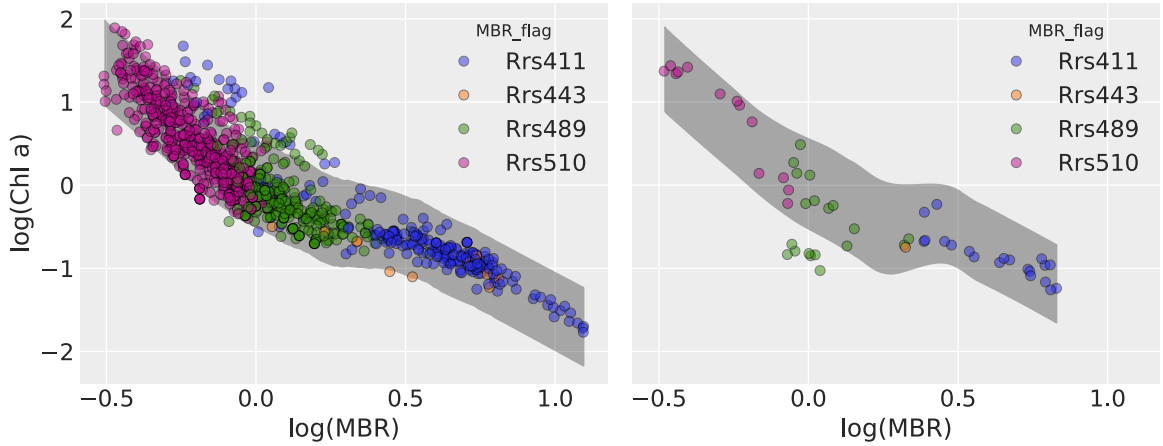

Figure S23: Model 3 predictive coverage. Left: in-sample (NOMAD). Right: out-of-sample (SeaBASS). Gray ribbons show the 94% posterior predictive HDI. Allowing group-specific dispersion produces visibly different interval widths across MBR numerator groups, aligning the HDI more closely with observed spread. In-sample coverage improves in the tails where Model 2 intervals were too uniform, while out-of-sample the persistent Rrs489 cluster remains below the HDI.

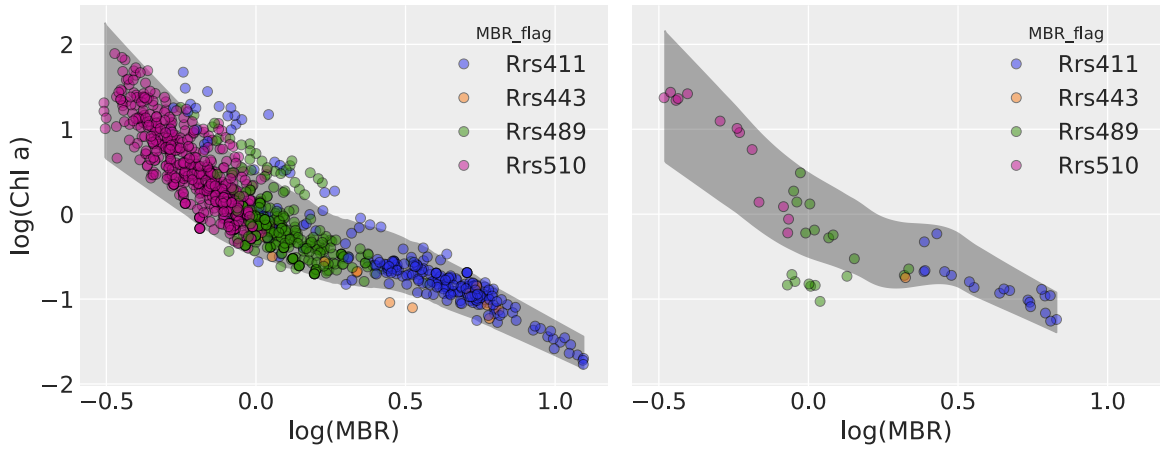

Figure S24: Model 4 predictive coverage. Left: in-sample (NOMAD). Right: out-of-sample (SeaBASS). Gray ribbons show the 94% posterior predictive HDI. Modeling dispersion as a function of log(MBR) produces a wedge-shaped envelope: intervals are much wider at low log(MBR) and narrow progressively with increasing values. This input-dependent variance structure yields closer alignment with observed spread across the predictor range. The out-of-sample panel (left) similar tightening of the HDI band.

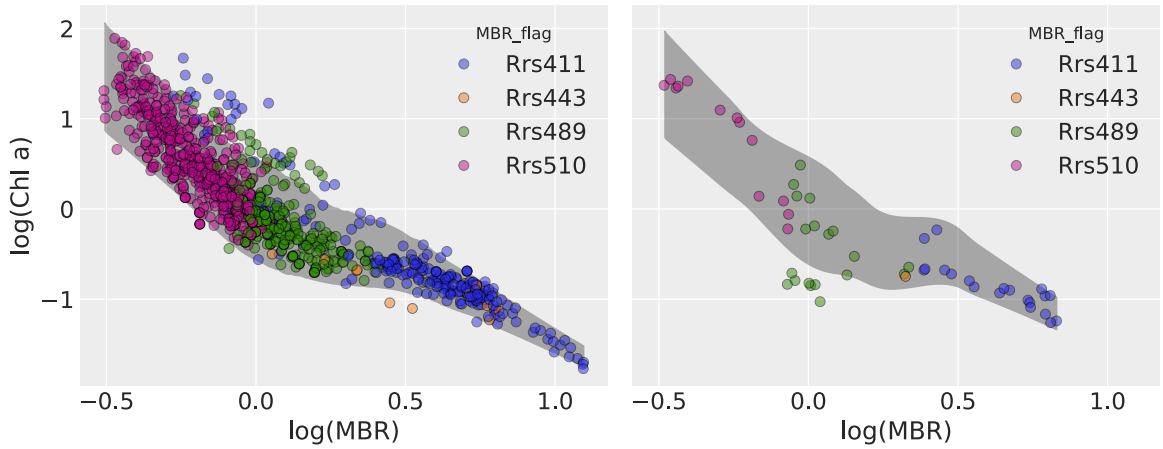

Figure S25: Model 5 predictive coverage. Left: in-sample (NOMAD). Right: out-of-sample (SeaBASS). Gray ribbons show the 94% posterior predictive HDI. Group-specific variance functions yield narrower and more flexibly shaped intervals than in Model 4, adapting to both slope and intercept differences across MBR groups. In-sample, the envelopes conform closely to each group's observed spread. Out-of-sample, coverage remains stable across groups, with predictive intervals transferring more effectively than in earlier models.

4. Five-Model Comparison

To evaluate predictive performance across all models, I used Pareto-smoothed importance sampling leave-one-out cross-validation (PSIS-LOO). This method approximates the expected log predictive density (ELPD) that each model would achieve when predicting unseen data, while adjusting for model complexity. Unlike point-based metrics such as RMSE or R^2, PSIS-LOO evaluates the entire posterior predictive distribution, providing a more comprehensive basis for comparison.

Table S1 summarizes the PSIS-LOO results for Models 1 through 5, with smaller rank values indicating better expected predictive accuracy. These numerical results are more clearly conveyed in Figure S26, which provides a visual representation of model ranking along with the associated uncertainty.

Table S1: PSIS-LOO comparison of Models 1 through 5. **rank**: model ranking based on expected out-of-sample predictive accuracy, with 0 indicating the best-performing model. **elpd_loo**: expected log predictive density; higher values indicate better predictive performance. **p_loo**: effective number of parameters, estimated from the variance of the pointwise log-likelihood; reflects model flexibility and complexity. **elpd_diff**: difference in ELPD relative to the top-ranked model; large positive values indicate substantially worse predictive performance. **weight**: approximate model weight under Bayesian stacking, representing relative support for each model given the data; values near 1 indicate strong preference. **se**: standard error of the ELPD estimate for each model. **dse**: standard error of the ELPD difference compared to the top-ranked model. **warning**: flag indicating whether reliability issues were detected in the importance-sampling diagnostics; `False` indicates stable estimates. **scale**: the unit in which predictive densities are expressed (here, log scale).

Model	Rank	ELPD_{LOO}	p_{loo}	ΔELPD	Weight	SE	dSE	Warning
Model 5	0	-0.25	15.27	0.00	0.96	28.11	0.00	False
Model 4	1	-51.73	10.87	51.48	0.00	29.98	10.43	False
Model 3	2	-111.06	14.63	110.81	0.00	27.95	13.41	False
Model 2	3	-114.00	9.88	113.75	0.00	27.59	12.54	False
Model 1	4	-144.54	5.40	144.28	0.04	31.67	21.66	False

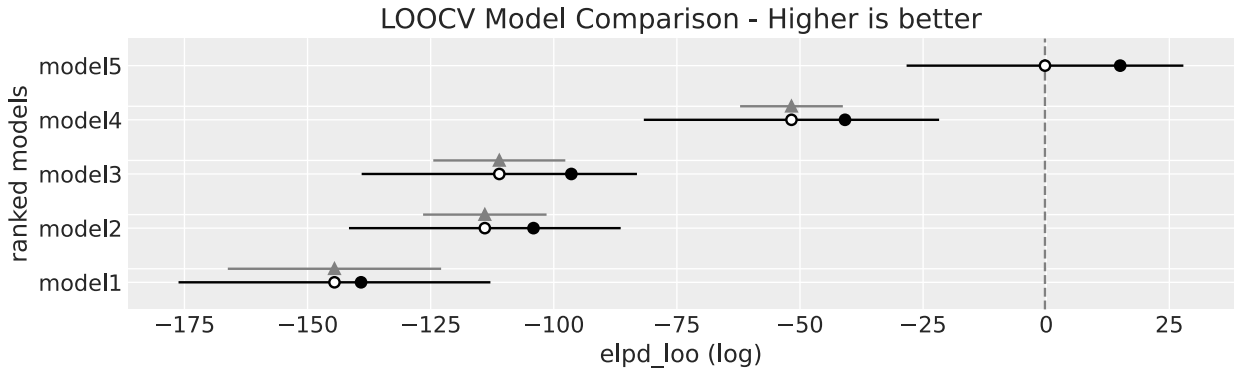

Figure S26: LOOCV model comparison (higher is better). The horizontal axis shows ELPD_{LOO} on the log scale; models are ordered top to bottom by rank (best at top). Open circles mark out-of-sample expected log predictive density estimated via PSIS-LOO; filled circles mark the corresponding in-sample predictive performance computed on the full dataset (same log-probability units), allowing direct visual comparison of apparent fit versus expected generalization. Horizontal error bars on the open circles are the SE of ELPD_{LOO} for each model. Light-gray horizontal segments (enabled by `ic_diff`) depict $\pm$dSE intervals for the ELPD differences relative to the top model (triangle at $\Delta = 0$), indicating the uncertainty in the pairwise gaps that drive ranking. Larger (less negative) ELPD values indicate better expected out-of-sample performance. When ΔELPD for a model is large relative to its dSE interval, the separation is practically decisive; when ΔELPD is on the order of its dSE, ranking uncertainty should be assumed.

Taken together, Table S1 and Figure S26 present a consistent view of model performance, with the table providing detailed numerical values and the figure highlighting both relative ranking and the uncertainty in those comparisons. The comparative rankings reinforce the

patterns seen in predictive coverage and LOO-PIT diagnostics, where progressively richer model structures yielded improved calibration and generalization.